ISSN 2079-1704. Himia, Fizika ta Tehnologia Poverhni. 2022. V. 13. N 1. P. 3-35

PACS: 68.03.Cd; 68.08; 68.08.Bc doi: 10.15407/hftp13.01.003

G.V. Beketov, O.V. Shynkarenko

SURFACE WETTING AND CONTACT ANGLE: BASICS AND CHARACTERISATION

V.E. Lashkaryov Institute of Semiconductor Physics of National Academy of Sciences of Ukraine
41 Nauki Ave., Kyiv, 03028, Ukraine, E-mail: gbeketov@ukr.net

Wettability is of pivotal importance in many areas of science and technology, ranging from the extractive industry to development of advanced functional materials and biomedicine problems. An increasing interest to wetting-related phenomena stimulates impetuous growth of research activity in this field. The presented review is aimed at the cumulative coverage of issues related to wettability and its investigation. It outlines basic concepts of wetting as a physical phenomenon, methods for its characterisation (with the emphasis on sessile drop techniques), and performances of contemporary instrumentation for wettability measurements.

In the first section, physics of wettability is considered. The intermolecular interactions related to wetting are classified as dependent on their nature. Thus, discussion of interactions involving polar molecules covers permanent dipole - permanent dipole interactions and freely rotating permanent dipoles. Consideration of interactions resulting from the polarization of molecules includes interactions between ions and uncharged molecules, Debye interactions, and London dispersion interactions. Hydrogen bonds are discussed separately.

The second section deals with the issues related to surface tension and its effect on shaping the surface of a liquid brought in contact with a solid body. The relationship between the surface tension and the contact angle as well as equations that quantify this relationship are discussed. The Young–Laplace equation governing the shape of the drop resting on the surface is analysed.

The third section is devoted to the experimental characterization of surface wettability and the underlying theoretical analysis. Particular attention is paid to the method known as the Axisymmetric Drop Shape Analysis (ADSA). Principles of automated determination of relevant physical values from experimental data are briefly discussed. Basics of numerical techniques intended for analysing the digitized image of the drop and extracting information on surface tension and contact angle are outlined.

In the fourth section, an overview of commercially available instrumentation for studying wettability and the contact angle measurements is presented. The prototype contact angle analyser designed and manufactured at the ISP NASU is introduced.

Keywords*: wettability, intermolecular interactions, surface tension, contact angle, sessile drop, Young–Laplace equation, axisymmetric drop shape analysis, contact angle goniometry, digital image contour extraction, methods of optimization*

INTRODUCTION

Over almost three past decades, the topic of wetting has generated an unprecedented growth of interest from both fundamental and applied points of view. The annual number of publications on wettability issues has increased by orders of magnitude during this period [1]. Current progress in development of advanced materials and technologies is largely based on achievements in chemistry, physics and technology of surface, which, in their turn, were attained due to advent of the contemporary methods of surface analysis [2]. The techniques of X-ray surface spectroscopy (XPS), secondary ion mass-spectrometry (SIMS), atomic force microscopy (AFM) *etc.* made available comprehensive information on chemical composition, morphology, reactivity, and many other characteristics of surfaces. Phenomenon of surface wettability also received a new impetus for further investigation, which stimulated both the improvement of theoretical models and the experimental techniques related to this area. Research efforts in this direction cover a huge variety of different fields ranging from the extractive industry (increasing the efficiency of the oil fields exploitation, ore mining and processing industry *etc*. [3–6]) to development of biocompatible materials [7–12] and studying the intricate interfacial biomolecular interactions realizing signalling pathways in the living organisms [13].

Wetting is a physical interaction of a liquid with the surface of a solid or with other liquid.

As an analysis of publications shows, there are at least two major reasons for the increasing interest to this phenomenon. One of them is that wetting plays important role in a vast array of modern technologies involving formation of coatings, use of adhesives, painting applications, soldering, brazing, *etc*. For example, wetting in combination with the surface tension enables formation of tiny solder bumps interconnecting the hybrid multielement focal matrices for infrared and ultraviolet vision [14–16]. Consequently, the degree of surface wettability, that is the ability or inability to wet, needs to be explained and quantified. The second reason arises from the need in a fast and inexpensive technique for monitoring the efficiency of various surface treatments. Modification of physical and chemical structure of the surface is widely used as the means to impart it certain functional properties. Any modification is highly likely to affect the surface wettability. Thus, it is possible to use the monitoring of wettability as a tool for experimental evaluation of modification efficiency. In this case, measurements of wettability become a helpful supplement to other techniques of surface analysis.

Wettability depends on interrelation between the adhesion and cohesion forces in the liquid-solid system. The cohesion forces are the forces of mutual cohesion of the molecules constituting the liquid, while the adhesion forces act between the molecules of the liquid phase and the wetted surface. The ratio of adhesion to cohesion forces results in effects that can be used to characterize wettability. If the cohesion forces significantly exceed the adhesion forces, the liquid drop on the solid surface tends to get a spherical shape, so minimizing the contact area. This situation corresponds to low wettability and occurs, for example, with a water drop deposited onto the surface of polysiloxane (silicone rubber). The opposite situation corresponds to predominance of adhesion forces over cohesion forces (high wettability). In this case, the fluid tends to spread out over the surface, and the contact area increases (at that, in both cases the acquired drop shape minimizes the free energy of the fluid-solid system).

The most popular approach to evaluation of surface wettability consists in analysing the shape of the drop that rests on the surface to be characterized. This approach is referred to as the sessile drop method [17], where a quantity to be determined is the angle between the surfaces of the liquid drop and the solid phase at the point where they meet. This angle, termed as the contact (or wetting), angle, is considered as the measure of surface wettability. The contact angle measurements have gained wide popularity due to their simplicity and robustness. Though the contact angle can also be measured in geometries that differ from the sessile drop geometry, the last one possesses important advantages in practical applications. In particular, only a small portion of the surface to be examined is enough to carry out the experiments. This enables wettability measurements for various finished products, such as dental implants, ophthalmic contact lenses, *etc*. [9–12]. In contrast, the vast majority of other methods, for example, the Wilhelmy plate method [18], require the use of specimens of a certain shape and size.

This review covers the basic issues related to research and practical applications of the wettability phenomenon. These issues include the nature and classification of intermolecular forces involved into wetting process, the effect of surface tension, the mathematical analysis of droplet shapes resulting from this effect, the techniques designed for characterization of surface vettability, and the modern instrumentation for the sessile drop measurements.

PHYSICS OF WETTABILITY

Wetting is generally understood to mean the spontaneous spreading of a liquid over solid surfaces or other liquids, the impregnation of porous materials and powders, and the curving of the liquid surface upon contact with a solid. The susceptibility to wetting is called wettability. The degree of wettability depends on the balance of cohesive and adhesive forces, respectively, between the molecules in the liquid phase and at the liquid-surface interface, which arise due to intermolecular interactions [19, 20]. In principle, wetting may involve chemical reactions between the liquid and the solid surface, interdiffusion and formation of surface layers, that is called a reactive wetting [21]. The reactive wetting is of huge importance for the soldering and brazing technologies [22, 23] and deserves separate consideration. The scope of this review is restricted to phenomena related to the non-reactive type of wetting that occur as a result of intermolecular interactions of purely physical

nature. The non-reactive wetting does not lead to the change in the chemical state of interacting molecules and is usually reversible. The reversibility of the non-reactive wetting is extensively used in experimental techniques intended for determination of wettability characteristics. Typically, water and organic solvents behave as the non-reactive wetting fluids. Wettability of solids by liquids is commonly quantified by a contact angle (wetting angle). The contact angle measures the tilt of the tangent to the liquid surface at the point where the liquid – gas/vapour interface meets the solid surface. The concept of cohesive and adhesive forces interpreted at a phenomenological level was employed by Young to deduce the value of contact angle for a given pair of liquid and a solid [24]. The modern understanding of intermolecular interactions has undergone radical transformation and refinement since publication of this pioneering work. The interactions that control wettability have been found to involve various mechanisms, which can differ as dependent on the nature of the wetting fluid and the wetted surface. However, it should be realized that the classification of intermolecular forces into a number of seemingly different categories is actually just a convenient scheme, while fundamentally they are of the same origin and stem from interactions between electrically charged particles constituting atoms and molecules. Thus, the common terms such as van der Waals forces, ionic bonds, hydrophobic interactions, hydrogen bonds, solvation forces *etc*. are the result of this classification rather than separate entities. Moreover, there is some ambiguity in the literature regarding the distinction between certain intermolecular interactions sharing similar features. Therefore, in order to maintain the consistency within the below consideration, we will follow the approach adopted in the classic textbook by J.N. Israelachvili [25]. This approach consists in dividing the interactions into groups according to characteristics of participating molecules, which includes the interactions involving polar molecules, the interactions involving the polarization of molecules, and the van der Waals forces acting between molecules. There exist, however, approaches that proceed from other principles when considering the intermolecular forces (see, for instance, [26]). In order to avoid misunderstanding, we will refer the reader to the corresponding sources, where appropriate.

Interactions involving polar molecules. Permanent dipole – ion interactions. The interaction energy between the molecules possessing a permanent dipole moment and the ions is determined by the Coulomb's potential and is given by the following expression:

$$w(\mathbf{r},\mathbf{u}) = -\frac{(ze)(\mathbf{u}\,\mathbf{r})}{4\pi\,\varepsilon_0\,\varepsilon\,r^3}. \qquad (1)$$

Here $\mathbf{u} = q\mathbf{l}$ is a vector representing the dipole moment of the molecule (l is the distance between electric charges q), e is the electron charge, z is the multiplicity of the ion charge, and the magnitude of the vector $\mathbf{r}$ is the distance between the ion and the centre of the dipole. For example, for two electronic charges $q = \pm e$ separated by $l = 0.1$ nm, the dipole moment is $u = (1.602\cdot10^{-19})(10^{-10}) = 1.6\cdot10^{-29}$ C·m, or 4.8 D. The unit of dipole moment is the Debye, where 1 Debye (D) is 3.336^{-10} C·m, which corresponds to two unit charges separated by about ~ 0.02 nm. Small polar molecules have dipole moments of the order of 1 D. Under normal conditions, the ion-dipole interaction is much stronger than kT at typical interatomic separations (0.2–0.4 nm). Thus, it is strong enough to bind polar molecules to ions and mutually align them when the ionic species are dissolved in polar solvents.

Permanent dipole – permanent dipole interactions. When the two polar molecules with no net charge but possessing a permanent dipole moment are considered fixed, the energy of their interaction can be deduced based on (1), where the single ion is to be replaced by the two separated charges of the opposite sign:

$$w(\mathbf{r},\mathbf{u}_1,\mathbf{u}_2) = -\frac{(\mathbf{u}_1\,\mathbf{u}_2)r^2 - 3(\mathbf{u}_1\,\mathbf{r})(\mathbf{u}_2\,\mathbf{r})}{4\pi\,\varepsilon_0\,\varepsilon\,r^5}. \qquad (2)$$

Here $\mathbf{u}_1$, $\mathbf{u}_2$ are the dipole moments of interacting molecules, and the magnitude of the vector $\mathbf{r}$ is the distance between the dipoles. The energy of the dipole-dipole interaction for a system of dipoles is the sum of the energies of all pairwise dipole interactions. Most dipolar molecules are also anisotropic in shape, making the point-like approximation for molecular dipoles inaccurate. For instance, the centres of two cigar-shaped molecules can come

significantly closer together when they align in parallel, thereby making this interaction more favourable. Strong orientational interactions between the molecules are accounted for within the theory of associated fluids [27].

The electric dipole-dipole interaction is not as strong as the ion-dipole interactions. For dipole moments of order approximately 1 D, it is weaker than kT at distances of about 0.35 nm in vacuum, while in a solvent medium this distance will be even smaller. This means that the dipole-dipole interaction, unlike the ion-dipole interaction, is usually not strong enough to result in any distinct mutual alignment of polar molecules in the liquid state. In this case the resulting interaction energy is to be calculated by appropriate averaging over all admissible configurations. However, there are some exceptions, which pertain to the molecules such as water, its small size and large dipole moment does lead to short-range association in the liquid.

Freely rotating permanent dipoles. Highly polar molecules with no net charge, such as water, HCl, HF, and NH_3 can interact dynamically if they are free to rotate. This interaction, known as the Keesom effect, comes about from the fact that on the average, two freely rotating dipoles will align themselves so as to result in an attractive force [28]. In order to calculate the net dipole-dipole interaction, it is necessary to examine all the possible orientations of the dipoles with respect to one another and consider what happens if the dipoles can reorient in each other's fields. To do so, it is convenient to rewrite expression (2) so as to represent the dependence of the interaction energy on the mutual orientation of dipoles evidently:

$$w(r,\theta_1,\theta_2,\varphi_{12}) = \frac{-u_1 u_2 \left(2\cos\theta_1\cos\theta_2 - \sin\theta_1\sin\theta_2\cos\varphi_{12}\right)}{4\pi\varepsilon\varepsilon_0 r^3} \tag{3}$$

The two dipoles are oriented with respect to the axis separating them along the angles θ_1, θ_2 and φ_{12} represents the angular orientation of one dipole with respect to the other about this axis. At large separations or high dielectric constant medium, the thermal energy would be greater than the interaction energy. At that, the interaction energy, averaged over all orientations, can be calculated using the Boltzmann distribution:

$$e^{-w(r)/kT} = \frac{\int e^{-w(r,\theta,\varphi_{12})/kT} \sin\theta\, d\theta\, d\varphi_{12}}{\int \sin\theta\, d\theta\, d\varphi_{12}} \tag{4}$$

where θ and φ_{12} vary between 0 and π and 0 and 2π, respectively, T is the absolute temperature and k is the Boltzmann constant. For $w(r, \theta, \varphi_{12})$ less than T, Eq. 4 can be expanded in terms of $1/T$ according to

$$e^{-w(r)} \approx 1 - \frac{w(r)}{kT} + \ldots \quad . \tag{5}$$

Upon averaging over θ_1, θ_2, and φ_{12}, it can be shown that $w(r)$ is given by

$$w(r) = -\frac{u_1^2 u_2^2}{3\left(4\pi\varepsilon\varepsilon_0\right)^2 kTr^6} \quad \text{for } kT > \frac{u_1 u_2}{4\pi\varepsilon\varepsilon_0 r^3} \quad . \tag{6}$$

This expression relates the interaction energy between freely (or almost freely) rotating permanent electric dipoles and their separation distances due to the Keesom effect. Qualitatively, the resulting attraction can be explained by the Boltzmann weighting factor that gives more weight to those orientations that have a lower (more negative) energy.

Interactions involving polarization of molecules. Molecular polarization is the emergence of a dipole moment induced by an external electric field. The polarization of molecules may occur through different mechanisms. For a nonpolar molecule, the polarizability arises from the displacement of its negatively charged electron cloud relative to the positively charged nucleus, known as the electronic polarizability. For polar molecules, there is another contribution to the polarizability. While for a freely rotating dipolar molecule the time averaged dipole moment is zero, the presence of an electric field will orient the dipoles, inducing in sum the non-zero polarization. The total polarizability of a polar molecule is given by the Debye-Langevin equation:

$$\alpha = \alpha_0 + u^2/3kT \, . \tag{7}$$

In a condensed liquid or solid medium consisting of many polarizable molecules, when the reaction fields of all the induced dipoles are added up, the resulting field is known as the

"polarization" field, E_p, which always opposes the inducing field E.

Interactions between ions and uncharged molecules. When a molecule of polarizability α is at a distance r from an ion of charge, ze, the electric field of the ion $E = ze/4\pi\varepsilon\varepsilon_0 r^2$ will induce in the molecule a dipole moment of

$$u_{ind} = \alpha E = \alpha ze / 4\pi\varepsilon\varepsilon_0 r^2 . \quad (8)$$

For small molecules like CH_4, the induced dipole moments can be of order of 1 Debye. Mutual orientation of the induced moment and the ion corresponds to arising an attractive force between them:

$$F(r) = (ze)E_r = -2\alpha(ze)^2 / (4\pi\varepsilon\varepsilon_0)^2 r^5, \quad (9)$$

that results in formation of a physical bond with the energy $w(r) = (\alpha E^2)/2$. This energy is half that expected for the interaction of an ion with a similarly aligned permanent dipole, because some energy is taken up in polarizing the molecule. For the ion in a solvent susceptible to polarisation, the ion – induced dipole interaction results in decreasing the Gibbs free energy, which can be estimated in terms of the Born energy [25].

Permanent dipole-induced dipole interactions (Debye interactions). The interaction between a polar molecule (a permanent dipole) and a nonpolar molecule susceptible to polarization (an induced dipole) can be described in analogy to the ion-induced dipole interaction just discussed by replacing a single ion with the two that form a permanent dipole. For a fixed dipole **u** oriented at an angle θ to the line joining it to a polarizable molecule, the interaction energy is

$$w(r,\theta) = \frac{1}{2}\alpha_0 E^2 = -u^2\alpha_0(1+3\cos^2\theta) / 2(4\pi\varepsilon\varepsilon_0)^2 r^6 . \quad (10)$$

For typical values of u and α_0, the strength of this interaction is not sufficient to mutually orient the molecules, as occurs in ion-dipole or strong dipole-dipole interactions. The effective interaction is therefore the angle-averaged energy. Since the angle average of $\cos^2\theta$ is 1/3, Eq. (10) becomes

$$w(r) = -u^2\alpha_0 / (4\pi\varepsilon\varepsilon_0)^2 r^6 . \quad (11)$$

More generally, for two molecules possessing both the permanent dipole moments u_1 and u_2 and polarizabilities α_{01} and α_{02}, their net dipole-induced dipole energy is

$$w(r) = -\frac{u_1^2\alpha_{02} + u_2^2\alpha_{01}}{(4\pi\varepsilon\varepsilon_0)^2 r^6} . \quad (12)$$

This is often referred to as the Debye interaction, or the induction interaction. It constitutes the second of three inverse sixth power contributions to the total van der Waals interaction energy between molecules, the first one being the Keesom force given by Eq. (6).

Instantaneous dipole – induced dipole interaction (London dispersion interactions). The types of physical forces described so far are fairly easy to understand, since they arise from straightforward electrostatic interactions involving charged or dipolar molecules. But there is another type of force that acts between all atoms and molecules, even totally neutral ones such as helium, carbon dioxide, and hydrocarbons. These forces have been variously known as dispersion forces, London forces, charge-fluctuation forces, electrodynamic forces, and induced dipole – induced dipole forces. They are referred below as the London forces.

The London forces constitute the third and perhaps most important contribution to the total van der Waals forces between atoms and molecules, because they are always present. Their main features may be summarized as follows:

1. They are long-range forces and, depending on the situation, can be effective from large distances (> 10 nm) down to interatomic spacing (~ 0.2 nm).

2. These forces may be repulsive or attractive, act both between the molecules and between larger particles, and in general do not follow a simple power law.

3. The London forces not only bring molecules together but also tend to mutually align or orient them, though this orienting effect is usually weaker than that with dipolar molecules.

4. The London forces are not additive. The force between two bodies is affected by the presence of other bodies nearby.

The London forces participate in a variety of fundamentally and practically significant phenomena including adhesion, surface tension, physical adsorption, wetting, the properties of gases, liquids, and thin films, and shaping the

structures of macromolecules such as proteins and polymers. The London forces are quantum mechanical in origin and are explained most rigorously within the frame of quantum electrodynamics. However, their origin may also be understood intuitively. The London forces can be thought to arise from the motion of electrons. The electrons in the molecules are in constant movement around the nuclei, which can spontaneously result in temporary uneven distribution of electric charges. This uneven distribution can create a temporary dipole, even on a non-polar molecule. The instantaneous dipole generates an electric field that polarizes any nearby neutral atom, inducing a dipole moment in it. The resulting interaction between the two dipoles gives rise to an instantaneous attractive force with the time average of this force being finite. A semiquantitative representation of mechanism giving rise to this force and the role played by the quantum mechanics can be deduced by considering a simple model based on the interaction between two Bohr atoms. In the Bohr atom the electron is pictured as orbiting around a proton. The smallest distance between the electron and proton is known as the first Bohr radius, a_0 at which the Coulomb energy, $e^2/4\pi\varepsilon_0 a_0$ is equal to $2h\nu$:

$$a_0 = e^2 / 8\pi\varepsilon_0 h\nu = 0.053 \text{ nm}, \quad (13)$$

where h is the Planck constant, and ν is the orbiting frequency of the electron. For the Bohr atom, $\nu = 3.3 \cdot 10^{15}$ cm^{-1}, so that $h\nu = 2.2 \cdot 10^{-18}$ J.

An instantaneous dipole of moment, $u = a_0 e$, will polarize a nearby neutral atom, giving rise to an attraction that is analogous to the permanent dipole – induced dipole (Debye) interaction discussed above. The energy of this interaction in a vacuum will therefore be expressed, in analogy with the Eq. (11), as

$$w(r) = -u^2 \alpha_0 / \left(4\pi\varepsilon\varepsilon_0\right)^2 r^6 = -\left(a_0 e\right)^2 \alpha_0 / \left(4\pi\varepsilon\varepsilon_0\right)^2 r^6, \quad (14)$$

where α_0 is the electronic polarizability of the second Bohr atom, which is approximately $4\pi\varepsilon_0 a_0^3$ (see [25] for more details). With the expressions for a_0 and α_0, the interaction energy can be written approximately as

$$w(r) \approx -\alpha_0^2 h\nu / \left(4\pi\varepsilon_0\right)^2 r^6 . \quad (15)$$

Except for a numerical factor, Eq. (15) is the same as that derived by London in 1930 using quantum mechanical perturbation theory. More information on London dispersive forces can be found in [29–32].

Hydrogen bonds. Comparing to many other fluids, water possesses unusual and unique properties including abnormally high boiling point, freezing point, surface tension, heat of vaporization *etc*. Similar abnormalities are characteristic also to fluids that consist of molecules with the functional groups containing hydrogen atoms: O^-–H^+, N^-–H^+, and F^-–H^+. This indicates that the presence of hydrogen atom may lead to some unusually strong and orientation-dependent bonds involved in the intermolecular interactions. To clarify this issue, L. Pauling implicated the concept of hydrogen bonds, which at first sight appeared to possess some covalent character [33]. This idea was further developed in a number of fundamental works [34–37]. According to modern concepts, the hydrogen bond (or H-bond) arises from the electrostatic attraction between the hydrogen (H) atom that is covalently bound to a more electronegative atom or group, and another electronegative atom possessing a lone pair of electrons. The H-bond is usually denoted Dn–H···Ac, where the solid line indicates a polar covalent bond, and the dotted (dashed) line designates the hydrogen bond (Dn and Ac are the donor and acceptor atoms of the H-bond, respectively). Depending on the nature of the donor and acceptor atoms, geometry of the interacting system, and the environment, the energy of a hydrogen bond can vary between approximately 4 and 160 kJ/mol [38–40]. This makes them somewhat stronger than a van der Waals interaction, and weaker than fully covalent or ionic bonds. This type of bond can occur in both inorganic and organic molecules. The H-bonds are responsible for supporting the double spiral structure of the DNA molecule. The interplay between empirical and theoretical approaches to the problem of an elusive notion of H-bonds is discussed in a historical outline [41].

As it has been already mentioned, the classification of intermolecular forces adopted in many literary sources may differ from that presented above. In particular, the Keesom interactions, the Debye interactions, and the London dispersion interactions are frequently

considered as the partial contributions to the total van der Waals forces arising from their sum [25, 28, 42]. Moreover, recent scientific advance essentially extends the existing classification of intermolecular interactions. Thus, in addition to well-known van der Waals forces, the hydrogen bonds, and the others discussed above, some more non-covalent interactions were revealed to be involved in bonding mechanisms inside and between molecules. They include the halogen bonds, the metal–ligand coordination, pi–pi interactions, cation/anion–pi interactions, classical Derjaguin–Landau–Verwey–Overbeek (DLVO) interactions and others [43, 44].

It is also worth noting that the descriptive models of intermolecular interactions discussed above are rather pictorial but somewhat simplified. They can be partially or completely abandoned by applying a more fundamental theoretical treatment [26, 45, 46]. Therefore, the reader of this review should not feel stunned if very different terms were encountered in some publications instead of the interaction models discussed here.

To date, the progress in the experimental techniques based on the scanning probe microscopy (SPM) made it possible to investigate the mechanisms of intermolecular interactions by the direct force measurements at the nanoscale. With the development of colloidal and bubble probes, SPM can serve as one of the most powerful techniques for nanomechanical quantification of interaction forces between the solid surfaces and the liquid media. The bubble/drop probe SPM technique allows for the direct measurement of the force exerted from the surface onto the cantilever-attached bubble or drop [44, 47].

Fundamental notion of intermolecular interactions is still under development. Some seemingly well-established ideas about the nature of intermolecular interactions observed in several specific cases have recently been refuted. For instance, it was long time believed that gecko's[1] famous ability of climbing up upon the mirror-like wall depends only on the van der Waals forces. However, it has been revealed recently that it involves also the acid-base interactions between the gecko's setal surface and the wall material [48, 49]. Investigation of the sapphire surface after a contact with the setae using interface-sensitive spectroscopy provided a direct evidence for involvement of interactions between polar lipid headgroups exposed on the setal surface and the hydroxyl groups present at the surface of sapphire.

Another example is the adhesion force between the conductive monomolecular sheets constituting the layered structure of graphene. Graphene is a two-dimensional carbon allotrope. It is composed of carbon atoms arranged in a honeycomb-like hexagonal structure that form a single graphene sheet. As it has been predicted theoretically by H. Casimir (1909–2000) in 1948, the two parallel and perfectly conducting plates placed in vacuum should experience attraction due to what is now referred to as the Casimir force [50]. The Casimir force is a fundamental quantum-mechanical relativistic phenomenon, which originates from the vacuum fluctuations of the electromagnetic field. It couples electrically neutral objects with or without permanent electric and/or magnetic moments. It has been now realized that the Casimir force is involved into mutual adhesion of graphene sheets [51–53].

The special attention in this review to the distinctive features of various intermolecular forces stems from the importance of understanding their nature for the experimental study of the wetting mechanisms discussed below.

SURFACE TENSION AND CONTACT ANGLE. LAPLACE EQUATION

This section discusses the role of intermolecular forces in shaping the surface geometry of a finite portion of liquid, particularly in the close vicinity of a contacting solid body. The following consideration is essentially based on the concept of surface tension. It is evident that the energy state of the molecules in the surface layer and in the bulk of a fluidic body is not equivalent. At the interface, the molecules are exposed to the action of attractive forces only from the neighbouring molecules located beneath the surface (Fig. 1 *a*). This action tends to minimize surface area that can be effectively accounted for as a tension within the surface layer, termed the surface tension. The effect of surface tension resembles the action of a stretched elastic membrane covering the surface of a liquid body.

[1] A small lizard belonging to the family *Gekkonidae*, found in warm climates throughout the world.

Surface tension can be defined in terms of both force and energy [54]. The first definition relates the surface tension γ to the force F exerted by the surface upon its side boundary l of unit length:

$$\gamma = \frac{F}{l}. \tag{16}$$

The unit of surface tension defined in terms of force is a Newton per meter (N/m). The second one defines the surface tension as the energy required to extend the surface of liquid by a unit area:

$$\gamma = \frac{F \cdot \Delta x}{l \cdot \Delta x} = \frac{W}{\Delta A}, \tag{17}$$

where W is the work of the surface tension force, and ΔA is the increment of surface area. In this case, the surface tension is expressed in Joules per square meter (J/m^2). However, the numerical values of surface tension in both cases remain the same.

Similar forces act also on the surface of solids. However, while the surface tension in liquid can affect the shape of a liquid body, the surface tension in solids manifests itself only by the energetic effect of the interaction with the contacting media. Therefore, when referring to solids, it is common to use a more general term surface energy, defined according to (17). More rigorously, the surface energy (surface free energy, interfacial free energy) is the energy required to expand the surface area of a body under constant temperature and pressure by a unit area. This "excess energy" is a result of the incomplete, unrealized bonding at the interface. The surface energy quantifies the disruption of intermolecular bonds that occurs when the surface is expanded. For the solids to be stable, the surfaces must be intrinsically less energetically favorable than the bulk of a solid (the molecules on the surface have more energy compared to the molecules in the bulk), otherwise there would be a driving force for the surfaces to be created on account of disappearing the bulk. The surface energy may therefore be defined as the excess energy at the surface of a material compared to the bulk, or as the work required to build an area of a particular surface.

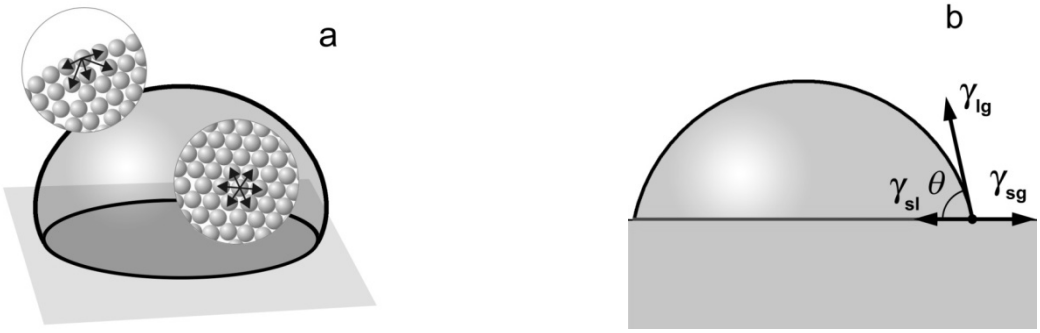

Fig. 1. Intermolecular forces between the molecules acting in the surface layer and in the bulk of a fluidic body (*a*). The shape of a sessile drop at the solid surface under equilibrium conditions. Here γ_{s1}, γ_{sg} denote the surface tensions at the solid-liquid and at the solid-gas (vapour) interfaces, respectively, and γ_{1g} is the surface tension of the solid-gas (vapour) interface. The contact angle measures the tilt of the tangent to the liquid surface at the point where a liquid – gas/vapour interface meets a solid surface (*b*)

The concept of surface tension is a convenient model for analyzing the shape of a finite portion of a liquid resulting from the action of intermolecular forces. As it has been already mentioned, a characteristic parameter of this shape is the contact angle. The contact angle measures the tilt of the tangent to the liquid surface at the point where a liquid – gas/vapour interface meets a solid surface (Fig. 1 *b*). The simplest way to access its value is direct measurement of the tangent angle at three-phase equilibrium interfacial point. This measurement can be performed using several different geometries of the liquid-vapour-surface system. Most common of them include the sessile drop technique, the captive bubble method, the Wilhelmy plate method, and the capillary rise at a vertical plate [54]. Among these methods, the

sessile drop technique currently has become one of the most extensively employed in wettability studies due to its convenience and versatility. Further improvement of this technique continues, and its several drawbacks noted in [54] have already been successfully overcome.

Consider the action of surface tension on the shape and the contact angle of a sessile drop, *i.e.* a liquid drop resting on a solid surface. Physically, the contact angle is determined by equilibrium between the surface tension and the adhesion forces between the liquid and the solid phase. Under the action of the first one, the sessile drop tends to take the shape of a truncated sphere, while the second one promotes spreading of the liquid over the surface. The relationship between the tension forces and the contact angle for the equilibrium drop shape is expressed by Young's equation [24, 55], derived in 1804:

$$\cos\theta = \frac{\gamma_{sg} - \gamma_{sl}}{\gamma_{lg}}, \qquad (18)$$

where cos θ is the contact angle, and γ_{1g}, γ_{s1}, γ_{sg} denote surface tensions of liquid-gas, solid-liquid, and solid gas, respectively. Note that the last two quantities were introduced rather formally, since they cannot be measured directly. This flaw was improved in the Dupré equation (see [56]) based on the balance of surface energies under the equilibrium conditions under constant temperature and pressure:

$$W_a = \gamma_{lg} + \gamma_{sg} - \gamma_{sl}. \qquad (19)$$

Here W_a is the reverse work of adhesion, that is, the reverse thermodynamic work of forces aimed at separating two dissimilar (heterogeneous) phases brought into contact, γ_{s1}, γ_{sg}, and γ_{1g} are, respectively, works of adhesion between the solid phase and the liquid, the solid phase and the gas (external environment), and between the liquid and the gas. The work of adhesion is related to the Gibbs free energy as:

$$W_a = -\Delta G^0. \qquad (20)$$

In the equilibrium state, the Gibbs energy has a minimum, so its derivative of the coordinate that describes the shape of the drop is equal to zero. This allows us to get rid of the inaccessible γ_{s1}, γ_{sg} and arrive at the Dupré – Young equation [54, 57–61]:

$$W_a = \gamma_{lg}(1 + \cos\theta). \qquad (21)$$

Unlike Young's equation, the Dupré – Young equation allows us to calculate the work of adhesion of a liquid to a solid, since the quantities (θ, γ_{1g}) included into this equation can easily be measured. This approach simplifies the system by reducing surface energy to a single number γ_{1g}, and excluding the other components, γ_{s1}, γ_{sg} from consideration.

It worth be noted that, despite the more than two centenary history of Young's equation, the problem of adequate theoretical description of surface tension still continues to be debated and refined till now. In particular, a careful examination of equation (19) shows that the component of surface tension γ_{1g} is not balanced (Fig. 1 *b*). This issue was discussed in [62–69]. Bikerman [64, 65] contended that if there is no opposite balancing force, the Young's equation is not valid (see also [66]). However, Bikerman did not take into account the strain field in the solid beneath the surface, which provided the needed balancing [67, 68]. Recently, more findings supporting the role of strain at the liquid-solid contact line and its effect on the wetting characteristics were presented [69, 70]. In these publications the strain of the elastic substrate or the rod under the influence of wetting force was directly observed and the role of this effect in behaviour of the contact line was discussed. Nevertheless, further debates still continue. A comprehensive review related to this topic is presented in [71].

There are also other reasons that require the equation representing the surface tension to be refined. The Young equation does not account for a layer of adsorbed molecules which inevitably present at the surface under regular conditions. Bangham and Razouk [61] highlighted the difference in the values of solid/vapour and solid/vacuum surface tensions as early as in 1937. More recently, the importance of adsorbed and wetting films covering solid surfaces has been generally recognized and widely discussed [72–83]. It was found that there is a transition region between the liquid phase and the substrate surface, which makes an additional contribution to the measured value of the contact angle. One of possible geometries of this region is shown in Fig. 2 (adopted from [79]). The effect of the transition region, which is now termed the contact line, can

be accounted for by introducing additional term in the Young equation [80–82]:

$$\cos\theta = \cos\theta_{\infty} - \frac{\gamma_L}{\gamma_{lg}}(1/r), \qquad (22)$$

where r is the radius of the liquid-solid contact area, θ_{∞} is the contact angle at the infinite radius, and γ_L is the line tension.

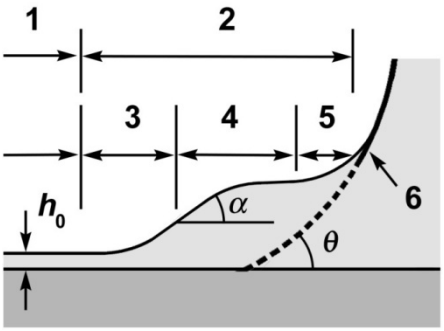

Fig. 2. Profile of film/meniscus transition zone: *1* – uniform film region; *2* – transition region; *3* – flat film; *3* – concave film; *4* – convex film; *5* – concave film; *6* – meniscus

The contribution from the line tension is especially important in case of nanodroplets, since the ratio between the contact line area and the drop surface increases along with decreasing the droplet volume. As the nanoscience has become one of hottest fields of research, the problems related to the role of the contact line in nanodroplet properties is currently attracting much attention [83–85].

Other modifications of Young equation outlined here were aimed at accounting for the micro- or nanoroughness of the solid surface, chemical inhomogeneity of the substrate and some other deviations from ideal surface conditions. A recent review [86] summarizes most significant issues related to wettability of imperfect surfaces. While Young's equation provides fundamental insights on wetting of flat surfaces, it has also been the basis of advanced wetting models on uneven surfaces: the Cassie-Baxter contact angle and the Wenzel contact angle [87–91].

The Cassie-Baxter contact angle relates to the chemically heterogeneous surface, where small (compared to the drop size) areas are characterized by different wettabilities. In particular, it can be applied to the porous surface when the pores are not wetted and remain filled with air. The Cassie-Baxter equation for contact angle can readily be obtained starting from the "energetic" interpretation of the Young's equation. Combining (19) and (20), for the case of the non-uniform surface we arrive at:

$$\Delta G^0 = -\gamma_{lg} + \sigma_1\left(\gamma_{1sl} - \gamma_{1sg}\right) + \sigma_2\left(\gamma_{2sl} - \gamma_{2sg}\right), \qquad (23)$$

where σ_1, σ_2 are the fractional areas of the two surface states that differ in wettabilities, and γ_{1sl}, γ_{1sg}, γ_{2sl}, γ_{2sg} are corresponding interfacial tensions of the solid-gas and the solid-liquid interfaces. This equation is analogous to (19) and, similarly to (18), results in:

$$\cos\theta_c = \sigma_1\cos\theta_1 + \sigma_2\cos\theta_2, \qquad (24)$$

known as the Cassie's law for heterogeneous surfaces [90].

The Wenzel contact angle is an "apparent" contact angle that characterises the rough surface. In the original article [91], it was deuced on the basis of "roughness factor" defined as

$$r = \text{roughness factor} = \frac{\text{actual surface}}{\text{geometric surface}}. \qquad (25)$$

This definition assumes that the actual surface of any real solid will be greater than the geometric surface because of surface roughness. Surface tensions, like specific energy values, are related to one unit of actual surface. But when liquid spreads over the surface of a real solid, the forces that oppose each other along a given length of the advancing periphery of the wetted area are proportional in magnitude to their total energies per unit of geometric surface. This must be true if surface tensions themselves are characteristic properties, unaltered by surface roughness. Thus, the Wenzel contact angle should be related to the Young contact angle as

$$\cos\theta_W = r\cdot\cos\theta_Y. \qquad (26)$$

The thermodynamic status of the Wenzel equation was discussed in [92]. It was explained and demonstrated by an example that the Wenzel equation may be incorrect. However, it was mathematically proven that the Wenzel equation correctly quantifies the apparent contact angle when the drop size becomes infinitely larger than the scale of roughness.

We broached just a few approaches of many others proposed for quantifying various phenomena associated with wetting and wettability. We have touched on them here as

they are relatively well established and ubiquitous. More recent trends in wettability research are characterized by increasing attention to wetting of "imperfect" surfaces, which demonstrate various peculiar effects. Thus, among the hottest topics today are the problems of superhydrophobic, superoleophobic and superhydrophilic surfaces, which have significant potential for practical use. The extraordinary properties of these surfaces are achieved by formation of micro- and nanoscale surface relief. An exhaustive survey of investigations in this direction is given in a recent review article [93]. In this work, the major challenges related to the use of the sessile droplet contact angle for characterizing surface wetting behaviour are reviewed. Different kinds of surface nonuniformity result also in the contact angle hysteresis (CAH) [94–96] (the hysteresis of the contact angle is the difference between the advancing and receding angles that typically depends on the surface geometries and degrees of wetting).

Many interesting examples of wetting and wettability in nature and technology are described in a recent textbook by E.Yu. Bormashenko [97]. This textbook introduces into the physics of surface wetting and its engagement for explaining phenomena of floating objects, condensation and evaporation of droplets, capillary waves, bouncing droplets, walking of water striders, and many other curious effects. In particular, Marangoni flows, surface tension inspired instabilities, liquid marbles, superhydrophobicity and super-oleophobicity (lotus effect) are considered. Many other aspects of wetting phenomena remain untouched here; however, the scope of this review does not leave more space for their consideration.

Young–Laplace equation. As follows from the above, the intermolecular interactions involved in wetting phenomena can be experimentally assessed by analysing the surface geometry of a finite portion of liquid contacting the solid body. The most characteristic feature of this geometry is the contact angle. Further discussion on surface geometry and contact angle requires consideration of pressure jump across curved liquid surface exerted by the surface tension. This jump, or the capillary pressure, determines the shape of droplet surfaces, liquid meniscus in a capillary tube, the geometry of a capillary rise at the contact with solid surfaces and provides a basis for interpretation of wettability-related experiments. A nonlinear partial differential equation that describes the capillary pressure difference sustained across the water-air interface (or between two static fluids), due to the phenomenon of surface tension (or thin wall tension), is known as the the Young–Laplace equation:

$$\Delta p = \gamma\left(\frac{1}{R_1} + \frac{1}{R_2}\right). \qquad (27)$$

This equation relates the pressure difference to the shape of the surface or wall in terms of surface tension γ and the principal radii of curvature, R_1 and R_2, which is fundamentally important for the study of static droplet and capillary surfaces. It represents a statement of normal stress balance for static fluids meeting at an interface, where the interface is treated as a surface (zero thickness). The equation is named after Thomas Young, who developed the qualitative theory of surface tension in 1805, and Pierre-Simon Laplace who completed the mathematical description in the following year. The Young–Laplace equation is often encountered in the literature covering the concepts of capillary pressure and wettability since it is quite general.

This equation may be derived either by requiring a force balance at the interface, or by considering the energy increment resulting from variation of interface geometry. A simplified derivation of the Laplace equation can be found, for instance, in [98]. However, a mathematically rigorous treatment requires familiarity with the properties of surfaces established in differential geometry. We outline here the approach to derivation of the Young-Laplace equation just conceptually, referring the interested readers to a more comprehensive elucidation (see [99]). For simplicity, we restrict ourselves to the quasi-one-dimensional case of the infinitely long elastic pipe. To determine the pressure jump between the inner volume of this pipe and the environment, consider first the force balance at its cross-section. Let the inner radius of the pipe be R (Fig. 3), the tension on the pipe wall be γ, and the length of pipe segment under consideration, dl be equal to unit. When the surface tension is defined as a mechanical force

per unit length, then the resultant of tension forces acting on the section of the pipe confined within the angle $d\varphi$ is $\gamma d\varphi$. At equilibrium, it should be equal to the force of pressure, $\Delta p\, R d\varphi$. This results in an equation

$$\Delta p = \gamma \cdot (1/R). \tag{28}$$

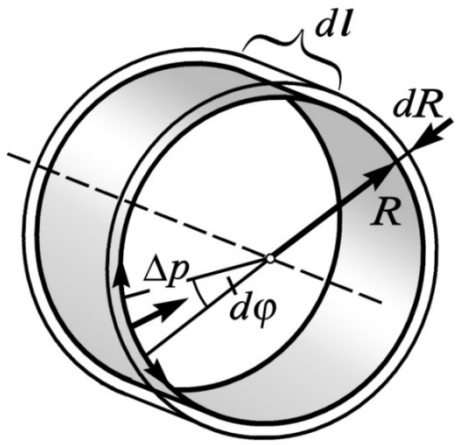

Fig. 3. To derivation of the Young-Laplace equation from consideration of the energy increment (the one-dimensional case)

Another approach consists in determination of the energy increment when inflating the pipe. Thermodynamically, the macroscopic surface energy is defined as the amount of mechanical work δW required to deform a surface in such a way that the total surface area changes by dA:

$$\delta W = \gamma d A. \tag{29}$$

Let the inner radius be increased by dR. Then, according to (29), the mechanical work will amount at $\gamma d A \equiv \gamma \cdot 2\pi d R = \Delta p \cdot 2\pi R \cdot d R$, resulting again in (28). Thus, both definitions are equivalent and can be used interchangeably depending on convenience.

For the above example, the longitudinal section of the pipe is a straight line with zero curvature. When the curvature is non-zero in two orthogonal directions, it can be expected that the pressure jump is a sum of contributions from both curvatures, thus yielding (27). This situation has been analysed in [98] in a similar way as the above by the example of an elastic spherical balloon. However, for a sphere, both radii of curvature are obviously equal and independent on the position by symmetry, thus limiting the generality of the results. In a general case of three-dimensional surfaces of arbitrary shape, two different radii of curvature, R_1 and R_2 are required to describe liquid surfaces. At any given point on the surface, they are defined by intersecting the liquid surface with two perpendicular planes, both containing the local surface normal. The resulting values of R_1 and R_2 will in general depend on the azimuthal orientation of the two surfaces. Rotating the two surfaces around the surface normal, a unique orientation can be reached, for which R_1 and R_2 attain a maximum and a minimum value, respectively. These maximum and minimum values are known as principal radii of curvature. The mean curvature, the specific combination

$$\kappa = \frac{1}{2}\left(\frac{1}{R_1} + \frac{1}{R_2}\right), \tag{30}$$

is a well-defined quantity, which determines the pressure jump across the liquid surface. With these definitions, the two-dimensional version of the Young–Laplace law reads as (27). This equation underlies the methods for calculating the surface geometry of a liquid body resulting from the combined action of surface tension and adhesion.

EXPERIMENTAL CHARACTERISATION OF SURFACE WETTABILITY. THE SESSILE DROP TECHNIQUE

Before discussing in detail the characterization of surface wettability by analysis of a sessile drop shape, we briefly outline and compare some most common techniques employed in this area of research. A general review of these techniques can be found in [100]. It is convenient to roughly classified them as “immediate”, based on a direct measurement of the force of surface tension, and “implicit”, where the wettability is quantified by analysis of experimental data involving the wettability characteristics indirectly.

The first group is represented mainly by the Wilhelmy method (Wilhelmy plate method) in various versions. This method was proposed by F.L. Wilhelmy in 1863 and consists in a direct measuring the downward pull exerted by a liquid upon a thin plate of solid material which is partially immersed [101] (Fig. 4). The plate is suspended from a balance arm. Its apparent weight will be the sum of the actual weight (in air) and the downward force exerted by the surface tension of the liquid with the deduction

of the buoyant effect of the displaced liquid. Obviously, the vertical pull depends upon the degree to which it is wet and hence upon the contact angle. A wide range of the research-grade instrumentation realizing this method is now commercially available (Fig. 5). Currently, Wilhelmy method is considered as one of the most reliable techniques for measuring contact angles on fibers of known dimension [102, 103].

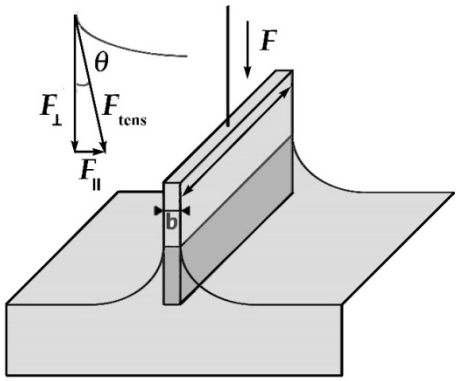

Fig. 4. The schematics of the Wilhelmy plate method (after [101])

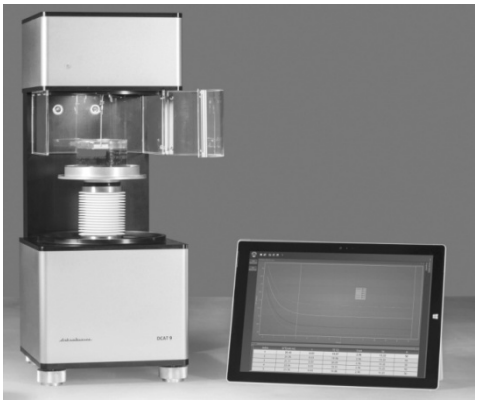

Fig. 5. Dynamic Contact Angle measuring device and Tensiometer DCAT-9 (DataPhysics Instruments GmbH, Germany)

Among the other group the first place is occupied by methods based on measuring the shape of the sessile drop [100, 104–106]. The basic scheme and a contemporary instrument designed for these measurements are shown in Figs. 6 and 7, respectively. The today's instrumentation for contact angle (CA) measurements combines high-resolution optics, exact liquid dosing, precise sample positioning, and computer-aided image processing into powerful and reliable measuring systems. The contact angle is derived from the drop image recorded by a video camera with the contour analysis software.

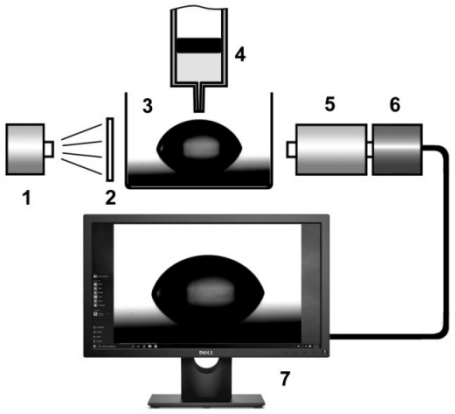

Fig. 6. Diagram of an arrangement for measuring the contact angle: *1* – light source; *2* – diffuser; *3* – sample chamber; *4* – syringe; *5* – telescope; *6* – video camera; *7* – monitor

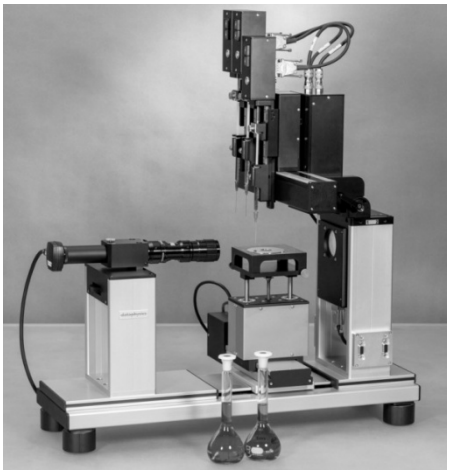

Fig. 7. Optical contact angle measuring and contour analysis systems OCA-50EC (Dataphysics Instruments, GmbH, Germany)

Other techniques that rely on measuring the curvature of a liquid surface in contact with a solid are capillary rise at a vertical plate [107] and a capillary bridge method. The first one exploits the capillary rise of a liquid brought in contact with a vertical and infinitely wide plate. The height of capillary rise, h, contact angle θ, and the surface tension γ are related by the equation

$$h = \sqrt{\frac{2\gamma_{lg}}{\Delta\rho g}(1-\sin\theta)}, \qquad (31)$$

where $\Delta\rho$ is the difference in density between liquid and gaseous environment, g is the

gravitational acceleration, and γ_{1g} is the surface tension of liquid-gas interface. The Wilhelmy balance method can be modified to measure the capillary rise h at a vertical plate in order to determine the contact angle θ [105, 106]. Dynamic contact angles are achieved by moving the plate up or down. This method has been widely used, and has proved to be particularly suitable for measuring the temperature dependence of contact angles [107–109]. Later, the Wilhelmy method has been automated by Budziak and Neumann [110]. For a specially prepared surface that forms a straight meniscus line, an accuracy of ±0.1° can be obtained. This technique also inherited most of the advantages and disadvantages of Wilhelmy balance method.

The capillary bridge method is a high-precision contact angle measuring technique, developed by Restagno *et al*. [111–113]. In their experiment, a spherical solid surface (usually a watch glass) is put in contact with a large liquid bath. Due to the capillary effect, a meniscus or "capillary bridge" forms around the contact line, which defines the wetted area on the solid surface (Fig. 8). The shape of this "capillary bridge" between the solid surface and the liquid changes as the solid is slowly moved up or down to give a systematically varying wetted area. By monitoring the changes of the wetted area and the distance that solid surface moves, the dynamic contact angles can be quantitatively determined through numerical resolution of the Young-Laplace equation or by a simplified approximated relation:

$$A = 2\pi R\left(k^{-1}\sqrt{2\left(1+\cos\theta\right)} - h\right) \qquad (32)$$

where A represents the wetted area, h is the distance of solid surface from liquid bath surface, R is the radius of the sphere surface, and k–1 is the capillary length, which is known for a given liquid. The contact angle θ can be deduced from the experimentally determined $A(h)$ curve.

The capillary bridge method offers several advantages. Both advancing and receding contact angles can be found by slowly pulling the surface away from the liquid or pushing back toward the liquid; thus, the dynamic contact angles can be studied. Due to its high sensitivity, the technique can be used to characterize surfaces with low contact angle hysteresis (of the order of 1°).

The simpliest technique that can be related to this group is the tilting plate method (not to be confused with the tilted plate technique). The tilting plate method developed by Adam and Jessop [114] was once favored due to its simplicity. In this method, a solid plate with one end gripped above the liquid is rotated toward the liquid surface until the end of the plate is immersed in the liquid, forming a meniscus on both sides of the plate. The plate is then tilted slowly until the meniscus becomes horizontal on one side of the plate. The angle between the plate and the horizontal is then the contact angle of interest. Some less common techniques were not mentioned here since they are more specific, or of lesser importance for the topic under consideration. More information on this topic can be found in [100, 104–106].

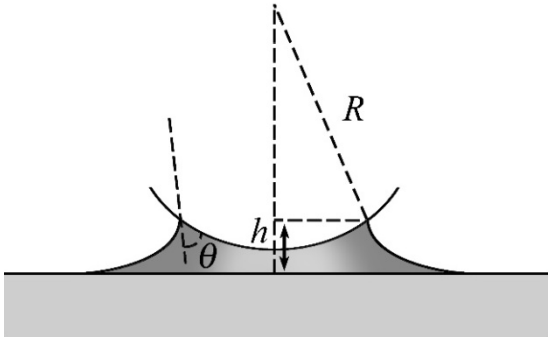

Fig. 8. Diagram of the contact angle measurements according to the capillary bridge method (after [100])

No single method can accommodate any kind of sample geometries, dimensions, or experimental conditions, but the most appropriate one can be selected in every situation. Among different methods, the advantage of the sessile drop technique is that it is the least dependent on the sample configuration and measurement conditions. Moreover, it has been demonstrated that it can be applied for contact angle measurements not only on a flat, but also on a curved surface [115]. This makes it the most popular approach to studying surface wettability.

Sessile drop technique: measuring contact angle. Direct measurement by telescope-goniometer. A technique for characterising the surface wettability by the contact angle measurement on a sessile drop profile was first introduced by Bigelow, Pickett and Zisman in 1946 [116]. Originally, it was intended for a

direct measurement of the tangent angle at the three-phase contact point of various liquids on polished surfaces. For this purpose, they suggested a simple and convenient instrument, which they referred to as a "telescope-goniometer". Later, the first commercial contact angle goniometer, designed by W.A. Zisman, was manufactured by ramé-hart instrument company in the early 1960s (Fig. 9). The instrument consisted of an adjustable optical stage for mounting a sample, a micrometer pipette to form a liquid drop, a light source, and a telescope equipped with a protractor eyepiece. These parts were assembled on an optical bench. The measurements were carried out by measuring the angle between the tangent to the drop profile and the surface of substrate at the contact point through the eyepiece by the protractor. The principle of the "telescope-goniometer" had proven to be very convenient due to its simplicity and versatility, and grown over the years into a powerful technique with greatly improved accuracy and precision. Contemporary instruments integrate video cameras, high quality objective lenses with adjustable magnification, computer-controlled motor-driven dosing syringes, enclosed temperature and atmosphere controlled sample compartment, powerful software for image analysis, and many other advanced features.

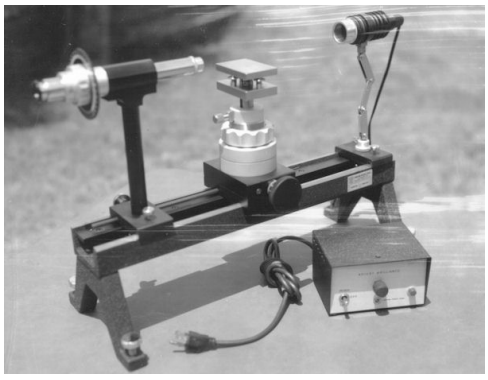

Fig. 9. Zisman's goniometer for measuring the contact angle manufactured by ramé-hart instrument company in the early 1960s

The direct goniometer method suffers from serious limitations. The accuracy and reproducibility of the measurement relies on the consistency of the operator in the assignment of the tangent line, which can lead to significant error and inconsistency between different users. Small contact angles (below 20°) cannot be accurately measured due to the uncertainty of assigning a tangent line when the droplet profile is almost flat. It is generally recognized that the direct measurement of sessile drop contact angles with a telescope-goniometer can yield accuracy not more than $\pm 2°$ [117, 118]. To overcome these and other issues, various approaches to computer-aided image analysis were developed to date.

Indirect contact angle measurements. The exact shape of the sessile drop as a whole is defined by the Laplace equation (27). Though there is no closed-form solutions of this nonlinear equations, it nevertheless imposes interrelations between certain generalized parameters characterizing geometry of the drop. Due to this, the contact angle can be derived indirectly from measured values of these parameters taken in appropriate combination. Potentially, this approach may result in a more accurate determination of the contact angle compared to direct measurements, provided the required parameters can be measured with sufficient precision.

This idea that lies behind the method for measuring the contact angle was proposed by G.H. Quincke (1834-1924) in 1870. The Quincke method was based on the observation that the height of a sessile drop resting on a horizontal substrate approaches a limit value as its volume is increased. In 1870, Quincke derived an approximate equation, now known as the Quincke relation, which relates the contact angle, θ_c with the height h of a large enough drop [119, 120]:

$$\theta_c = \cos^{-1}\left(1 - \frac{\rho g h^2}{2\gamma}\right). \qquad (33)$$

In this equation, g stands for the acceleration of gravity, ρ is the density, and γ is the surface tension. The method is particularly accurate when measuring the height of an extended liquid front because in this case the surface curvature resides entirely in the vertical plane and Eq. (33) is satisfied exactly. However, with the advent of more powerful techniques, the Quincke relation was gradually abandoned in the latter half of the 1920^s and emerged anew only in a text of 2004 [121]. Moreover, this method was essentially improved by F. Behroozi [122] who employed laser-assisted technique to detect a state of

complete flatness attained by the top surface of the drop while enlarging its size.

Another simple method for indirect determination of contact angle, known as half-angle method, was described in [123]. The idea of this method is underpinned by the assumption that the sessile drop is a spherical cap in shape (a spherical segment of one base, *i.e.*, bounded by a single plane). The cross section passing through its axis of symmetry is shown in Fig. 10. It can be proven within the frame of the plane trigonometry that the angle between the base of the cap and the segment connecting the triphase point with its top is half of the contact angle (the triphase point is the point where the arc of the cap section joins the base). Thus, having measured the height and the base length of the cap, the contact angle could be obtained from the expression:

$$\theta_c = 2 \cdot \arctan\left(\frac{2h}{l}\right). \tag{34}$$

However, as it has been noted above, this expression is valid only for exactly spherical cup, that is when the droplet is small enough for not to be distorted by gravity. However, with decreasing the drop size the contribution from the line tension discussed in section 2 (see Fig. 2) increases, influencing the obtained value of the contact angle.

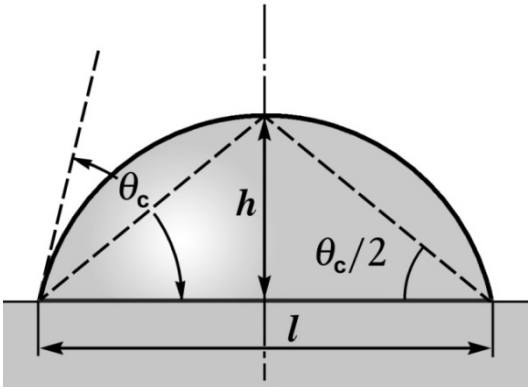

Fig. 10. The cross section of a sessile drop illustrating a half-angle method for determination of contact angle

In 2019, F. Behroozi and P.S. Behroozi proposed a more elaborated approach to determination of contact angle from the experimental contour of the sessile drop [124]. Instead of solving the Laplace equation, they resorted to an ingenious solution, setting the droplet volume with the use of an "analog device", namely using a high-precision dosing pipette. With a known volume of the droplet, the determination of the contact angle was reduced to measuring the droplet height and the footprint radius, which could be done with sufficiently high accuracy.

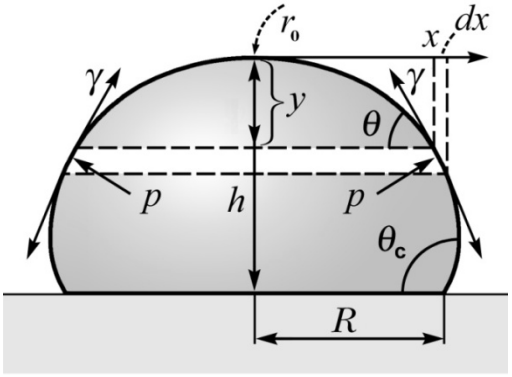

Fig. 11. The profile of a sessile drop resting on a flat surface. The surface band of infinitesimal width encircling the drop is shown between the dashed lines (after [126])

To derive governing equations for the drop shape, they considered equilibrium conditions for an infinitesimal surface belt encircling the drop (Fig. 11). The pressure at the base level of the shaded section of the drop is

$$p = 2\gamma / r_0 + \rho g y\,. \tag{35}$$

The first term is the pressure jump due to surface tension (note that the two principal radii of curvature at the apex are degenerate and equal to r_0), and the second term accounts for gravity (g is the acceleration of gravity, and ρ is the density of liquid). The balance of forces acting on the surface band in the vertical direction is given by the following equality:

$$\left(\frac{2\gamma}{r_0} + \rho g y\right) \cdot 2\pi x\, dx + 2\pi x \gamma \sin\theta = \\ = 2\pi\gamma\left(x + dx\right)\sin\left(\theta + d\theta\right). \tag{36}$$

In the limit of $d\theta \to 0$, they obtained after transformation the set of two parametric equations describing the droplet contour:

$$\frac{dx}{d\theta} = \frac{\gamma \sin\theta}{\left(\frac{2\gamma}{r_0} + \rho g y\right) - \frac{\gamma}{x}\sin\theta} \tag{37}$$

and

$$\frac{dy}{d\theta} = \frac{\gamma \sin\theta}{\left(\frac{2\gamma}{r_0} + \rho g y\right) - \frac{\gamma}{x}\sin\theta} \qquad (38)$$

(the second of these equations follows from the equality $dy/dx = \tan\theta$ that is fulfilled along the contour of the drop). An auxiliary equation gives the drop volume:

$$V = \int_0^h \pi x^2 \, dy \, . \qquad (39)$$

The system of differential equations (37), (38) can be integrated numerically, starting from the drop apex ($\theta = 0$), to obtain $x(\theta)$, $y(\theta)$, and the profile curve $y(x)$ when the parameters r_0, γ, and R are known. In order to obtain θ_c, the integration is to be terminated at the end point of the profile curve where the drop volume given by (38) reaches the experimentally preset value V_0. As it is difficult to measure the parameter r_0 precisely, the authors resorted to an iterative process, setting the starting value r_0 to h and comparing the resulting parameter V with the preset value V_0. With proper adjustment of r_0 from iteration to iteration, the condition of $V = V_0$ is finally fulfilled with the required accuracy. At this point, the iterations are terminated with the parameters θ_c and, additionally, r_0 being determined. The iterative procedure employed in this research actually belongs to a spacious domain of numerical techniques known as methods of optimization. An introductory course into these methods was written by Brian D. Bunday [125]. In this book, the most popular optimisation methods (The Hooke-Jeeves algorithm, also known as "pattern search", the Davidon-Fletcher-Powell penalty function method, the Fletcher-Reeves conjugate method, and some others) are described and supplemented with the source program codes.

We have considered several well-known methods for determining the contact angle from the experimentally obtained image of the droplet contour. The authors of these methods sought reducing the number of parameters to be measured in order to simplify the experiment. However, the price for this simplification was the requirement for high measurement accuracy, since errors are not compensated in any way and significantly affect the result. Information on several other similar methods that have not been discussed here can be found in the cited literature. With the widespread use of automation tools for experiments, the simplification of measurements has lost its relevance, and the main criterion for the effectiveness of the method has become an increase in accuracy. A priori, the best accuracy will be achieved if the calculations will fully take into account the entire array of obtained experimental data. Thus, we proceed to consideration of the currently most relevant approach to determining the contact angle, known as the Axisymmetric Drop Shape Analysis (ADSA), which was developed by Y. Rotenberg, L. Boruvka, and A.W. Neumann in early 1980 [126]. In view of its importance, special attention will be paid to the mathematical foundations of this method.

Axisymmetric Drop Shape Analysis (ADSA).

Whereas the experimental methods outlined above were aimed at determining the contact angle as a purely geometrical quantity, ADSA exposes also a related physical meaning. Development of ADSA was aimed at creating a technique capable of the overall drop shape analysis. This approach promised to improve radically the accuracy of contact angle determination compared to the methods, which rely on the measurements of only a few preselected characteristic points. A distinctive feature of the ADSA technique is that it accounts for the distortion of a drop by gravity. Actually, the gravity serves there as a built-in standard enabling quantification of the surface tension on the basis of the experimentally observed drop distortion. This feature is especially helpful when using different liquids with different surface tension for studying the dependence of wettability on the chemical structure of the surface. Otherwise, it would be impossible to bring into correlation the contact angle difference for fluids differing by molecular mechanisms of liquid-surface interactions (the last is of special importance when studying the chemical modification of solid surfaces).

The ADSA analysis is based on the solution of the Laplace equation, modified to take into account the forces of gravity. As it was discussed above, the Laplace equation (27) relates the pressure jump across a liquid-air (or liquid-vapour) interface with the curvature of the liquid

surface. To account for the contribution from the gravity force to this pressure difference, an additional term dependent on the elevation was added:

$$\Delta P = \Delta P_0 + \rho g z \,. \tag{40}$$

Here ΔP_0 is the pressure difference at a selected reference plane, ρ is the density of the liquid phase, g is the gravitational acceleration, and z is the vertical height measured from the reference plane. With the addition of the gravity term, the Laplace equation takes the following form [126, 127]:

$$\gamma\left(\frac{1}{R_1}+\frac{1}{R_2}\right) = \Delta P_0 + \rho g z \,. \tag{41}$$

A manageable solution of this equation can be obtained (using numerical techniques) for the case of the axisymmetric problem. This case applies to the liquid drop lying on a flat uniform horizontal surface, where it acquires the axially symmetric shape under the pressure of the surface tension. The axial symmetry imposes interrelation between the radii of curvature, R_1 and R_2, making them mutually dependent. This dependence fundamentally facilitates the solution of the Laplace equation for calculating the droplet shape. However, the rigorous consideration of the drop geometry is essentially based on the results of differential geometry, which are usually omitted in publications devoted to physics of wetting phenomena. In order to give the reader a more profound understanding of underlying mathematics, we will try to fill this gap here rather in an intuitive way.

First, we should refine the definition of the surface curvature. The intersection of the surface with a plane that contains a normal of this surface is called the normal section curve. The Euler's theorem [128] establishes the existence of principal curvatures and associated principal directions on the surface in which the curvature of normal section attains its the most and the least values. The Euler's theorem asserts that the vectors ξ_1 and ξ_2 lying in the principal directions are mutually perpendicular and that, moreover, if $\mathbf{X}$ is any vector making an angle θ with ξ_1, then the curvature κ_x along this $\mathbf{x}$ direction is given by

$$\kappa_x = k_1 \cos^2\theta + k_2 \sin^2\theta \,. \tag{42}$$

Here the quantities k_1 and k_2 denote the principal curvatures**.** The theorem is named for Leonhard Euler who proved it in 1760. The proof of this theorem at a level not burdened with modern mathematical terminology and notation is given in the textbook [129] available at a public domain through the Internet. The equality (42) results in a remarkable conclusion: curvatures of any mutually perpendicular normal sections $\mathbf{x}_1$, $\mathbf{x}_2$ give in sum the mean curvature of the surface at the point of their intersection. Taking into account that in this case the angles θ_1 and θ_2 between these sections and the principal direction ξ_1 differ by $\pi/2$, we obtain for the corresponding curvatures:

$$\kappa_{x1} = k_1 \cos^2\phi_1 + k_2 \sin^2\phi_1,$$

$$\kappa_{x2} = k_1 \sin^2\theta_1 + k_2 \cos^2\theta_1 \,. \tag{43}$$

Thus, it is evident that $\kappa_{x1} + \kappa_{x2} = k_1 + k_2$. This result makes it possible to calculate the mean curvature of the surface using any arbitrary normal sections provided they are mutually perpendicular.

The most natural coordinates on the surface of the axisymmetric drop are the meridians and the local arcs normal to the meridians at the surface point under consideration, as shown in Fig. 12. It is convenient to place the origin of the r-z coordinate system at the apex of the drop and to direct the z coordinate axis down along its axis of symmetry. In this case, the r-axis appears to be tangent to the curved interface at the drop apex, R_1 turns along the meridian, and R_2 lies in the plane normal to the meridian. In this geometry, it becomes possible to reduce the Laplace equation (that actually is a partial differential equation for the surface) to the ordinary differential equation (ODE) for the droplet generatrix with a single independent variable z and one unknown $r(z)$. For this, it is necessary to find a relationship between the radii R_1 and R_2, imposed by the axial symmetry of the drop.

Construct a circular conical surface tangent to the droplet surface, as shown in the Fig. 13 *a*, *b*. Let the plane S intersect the cone at some point of contact with the droplet surface perpendicular to the cone generatrix. Then the secant plane S forms the normal section perpendicular to the meridional one. Thus, as follows from (43), the curvatures of this section

and the meridional section of the drop enable calculation of the mean curvature. To perform this calculation, we resort to analytical geometry that establishes multifarious interrelations between the geometric properties of conics. In fact, we will need only two of them, the property referred to as an eccentricity, and the parameter a introduced later.

The conical section (a conic) may form three types of curves, dependent on the slant angle of the cone. The quotient $e = \cos\psi/\cos\theta$ gives the eccentricity of the conic. Here ψ is the angle between the secant plane and the cone axis. When the secant plane is normal to the generatrix, then $\psi = \pi/2–\theta$, and the elliptical, parabolic, and hyperbolic conics correspond to the angles $\theta < \pi/4$, $\theta = \pi/4$, and $\theta > \pi/4$, respectively. Note that in the literature the formula for eccentricity of conics often is given in a different form:

$$e = \sin\alpha/\sin\beta . \qquad (44)$$

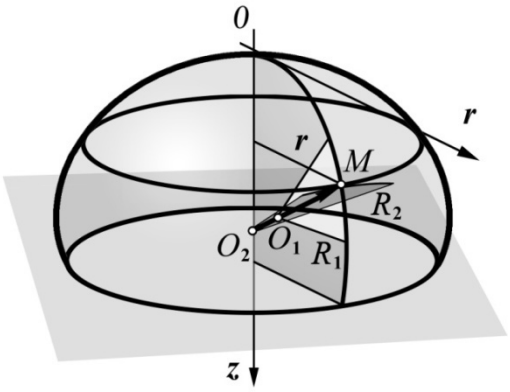

Fig. 12. Definition of the coordinate system of axisymmetric drop. Radius R_1 (segment O_1M) rotates in the meridional plane (lightened), radius R_2 (segment O_2M) rotates in the plane of normal section (shadowed)

This results from an alternative choice of the angles characterizing the eccentricity (Fig. 13 *a*), for which $\alpha = \pi/2–\psi$ and $\beta = \pi/2–\theta$ (see [129–131] for details).

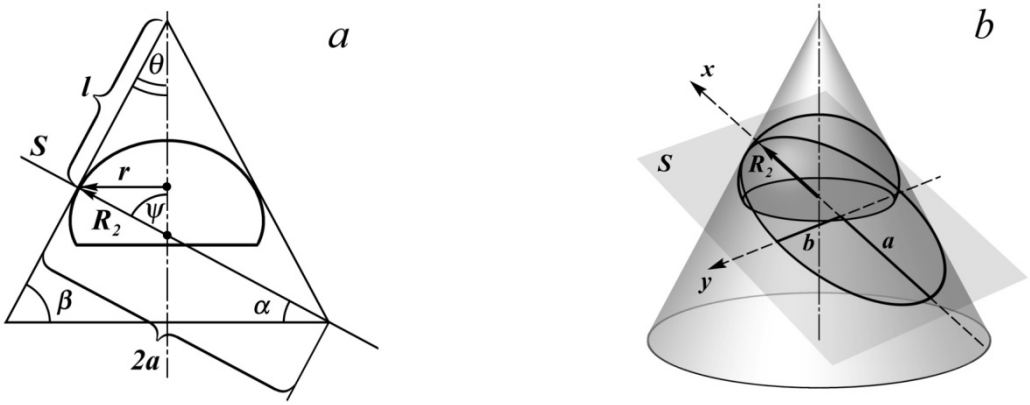

Fig. 13. To derivation of expression for radius R_2. The meridional section of a drop with the normal section S is shown in panel (*a*), and the correspondent 3D view is displayed in (*b*)

It is convenient to proceed further with the rectangular equations of conics in the Cartesian coordinates, taking the y-axis coincident with the directrix and passing the x-axis through the focus (see [131]). Then the equation

$$(1-e^2)x^2 + y^2 - 2kx + k^2 = 0 \qquad (45)$$

represents any conic (here k is the distance between the focus and the directrix). This equation can be further reduced to a canonical form. The canonical equations of different conics are:

$$\frac{x^2}{a^2} + \frac{y^2}{b^2} = 1 \text{ for ellipse,} \qquad (46)$$

$$\frac{x^2}{a^2} - \frac{y^2}{b^2} = 1 \text{ for hyperbola,} \qquad (47)$$

$$y^2 - 2px = 0 \text{ for parabola.} \qquad (48)$$

For ellipse, a and b are half-lengths of its width and the height (a semi-major and semi-minor axes). For hyperbola, a is half-distance between its apical points, and b defines the incline of the asymptotes:

$$y = \pm \frac{b}{a} x . \quad (49)$$

For parabola, p is the distance of the focus from the directrix.

The eccentricities of conics in terms of a and b are given by the following expressions:

If the conic is a parabola,

$$e = 1; \quad (50)$$

if the conic is an ellipse,

$$e = \sqrt{1 - \frac{b^2}{a^2}}; \quad (51)$$

and if the conic is a hyperbola,

$$e = \sqrt{1 + \frac{b^2}{a^2}} . \quad (52)$$

The eccentricity e of the ellipse has a visual meaning, characterizing the degree of its elongation in comparison with a circle. The detailed explanation of the above formulas can be found in references [130–134].

Below we consider as an example a relationship between the radii R_1 and R_2, for the elliptical conical section. Other types of conics can be treated in a similar way. The radius R_2 is the radius of curvature at the end of the major axis of the ellipse [134]:

$$R_2 = b^2 / a . \quad (53)$$

From this, the radius R_2 can be expressed through the cone angle θ (Fig. 13 *a*). Let us denote the distance from the top of the cone to the line of contact with the surface of the drop as l. Then the length of the semi-major axis a can be expressed through l and the angle θ:

$$\frac{2a}{l} = \mathrm{tg}(2\theta) = \frac{2\,\mathrm{tg}\,\theta}{1 - \mathrm{tg}^2\,\theta} . \quad (54)$$

If the generatrix of the cone is normal to the secant plane, then the angle ψ is $\pi/2–\theta$, and $\cos\psi = \sin\theta$. Then the equality (44) turns to $e = \tan\theta$. Substitution of this equation to (51) gives:

$$\frac{b^2}{a^2} = 1 - \mathrm{tg}^2\,\theta . \quad (55)$$

Multiplying the left and right sides of equation (54), respectively, by the left and right sides of equation (55), we obtain:

$$\frac{2a}{l}\frac{b^2}{a^2} = \frac{2\,\mathrm{tg}\,\theta}{1 - \mathrm{tg}^2\,\theta}\left(\mathrm{tg}^2\,\theta - 1\right),$$

or, after reducing,

$$\frac{b^2}{a} = l \cdot \mathrm{tg}\,\theta = \frac{l \cdot \sin\theta}{\cos\theta} = \frac{r}{\cos\theta} . \quad (56)$$

Substitution of expression for R_2 (53) into (56) yields:

$$R_2 = \frac{r}{\cos\theta} . \quad (57)$$

Taking into account (57), the equation (27) can then be rewritten as:

$$\gamma\left(\frac{1}{R_1} + \frac{\cos\theta}{r}\right) = \frac{2\gamma}{R_0} + \rho g z . \quad (58)$$

We arrived at the equation for the meridional contour of sessile drop given in [126] (except for the definition of the angle θ). Here ΔP_0 is expressed by the Laplace equation through R_0, the radius of curvature at the apex of the drop (at the apex, both radii of curvature, R_1, R_2 become equal due to the symmetry of this configuration). Before switching to solution of this equation, the choice of the appropriate drop size for ADSA experiments is to be discussed.

As explained above, the efficiency of the ADSA approach depends on a balance between the surface tension and the gravity that determines the deviation of the drop shape from the sphere. The importance of gravitational forces can be assessed by the magnitude of the dimensionless parameter called the Eötvös number (Eo), also known as the Bond number (Bo) [135, 136]. These two names commemorate the Hungarian physicist Loránd Eötvös (1848–1919) and the English physicist Wilfrid Noel Bond (1897–1937), respectively. This number is defined as:

$$Eo \equiv Bo = \frac{\rho g L^2}{\gamma} , \quad (59)$$

where ρ is the density of the liquid in the drop, L is the characteristic length of the drop (that can be estimated from the drop volume V), and γ is the surface tension of the interface between the drop and the ambient phase. Another frequently used formula for the Bond number is:

$$Bo = \left(\frac{L}{\lambda_c} \right)^2, \quad (60)$$

where $\lambda_c = \sqrt{\gamma/\rho g}$ is the capillary length. In the limit of small Bond number, the shape deviation due to gravity is negligible, and the interface shape can be approximated as a spherical cap. This approximation permits analytical solutions for the drop configuration. When $Bo \sim 1$, the forces of surface tension and gravity become comparable, resulting in a distortion of the drop. This arises at a length scale commensurable with the capillary length. For an air-water surface, for example, $\gamma \approx 70$ dynes/cm, $\rho = 1$ g/cm^3 and $g = 980$ cm/s^2, so that $l_c \approx 2$ mm. Within this domain the ADSA approach is most effective.

Since the equation (58) can be solved only by numerical techniques, the most common way to extract physical parameters from the experimental results using ADSA method involves fitting procedures. The general scheme of the fitting method consists in finding a numerical solution to the equation, which depends on some fitting parameters, determining the discrepancy between the found solution and the experimental result, and achieving their coincidence by varying the fitting parameters.

Calculation of the drop contour $r(z)$ requires that the equation (58) be reduced to the ODE form. In general, this can be done in different ways depending on the selected solving method and the appropriate coordinate system. Thus, an analogous equation that describes the meniscus shape $r(z)$ reduced to the Cartesian coordinates r, z for the capillary rise of liquid was given in [54, 137.]

$$\rho g z = \gamma \left(\frac{z_r''}{\left[1 + (z_r')^2\right]^{3/2}} + \frac{z_r'}{r\left[1 + (z_r')^2\right]^{1/2}} \right). \quad (61)$$

Here the first term in the brackets is a standard expression for the curvature of a plane curve defined by the function $z(r)$ [138], that replaces the curvature given above in term of $1/R_1$. The expression for the second term follows from the trigonometric formula $\cos\theta = 1/\sqrt{1+\tan^2\theta}$, taking into account that $\tan\theta = 1/z_r'$. However, the direct use of the equation (61) for ADSA is aggravated by the ambiguity of solution when the contact angle exceeds $\pi/2$ (the case of poor wettability). Thus, consider the approaches to numerical solving the equation (61).

A representation of the sessile drop contour that is more suitable for calculations can be obtained by converting the equation (61) into a parametric form, according to [126]. Assuming $x = x(s)$ and $y = y(s)$ with s being the arc length measured from the top of the drop (Fig. 13 *a*), we get:

$$\frac{dx}{ds} = \cos\psi, \quad (62)$$

and

$$\frac{dz}{ds} = \sin\psi, \quad (63)$$

where variables have the same meaning as in Fig. 12. By definition,

$$\frac{1}{R_1} = \frac{d\psi}{ds}. \quad (64)$$

Combining (58) with (64) yields

$$\frac{d\psi}{ds} = \frac{2}{R_0} + \frac{\rho \cdot g}{\gamma} z - \frac{\sin\psi}{x}, \quad (65)$$

where cos θs replaced with sin ψ. Equations (62), (63), and (65) with the boundary conditions

$$x(0) = z(0) = \psi(0) = 0 \quad (66)$$

form a set of first-order differential equations for x, z, and ψ, as functions of the argument s. For given R_0 and given $\rho g/\gamma$ the complete shape of the curve may be obtained by integrating simultaneously these three equations. In [126], the solution of this set of equations was obtained using a numerical procedure by minimising the objective (or target) function defined as:

$$F_N = \sum_{n=1}^{N} \left[\delta(u_n, v_n) \right]^2 \quad (67)$$

(see Fig. 14). This definition represents the objective function in the form that completely conforms to the generally accepted approach. However, its calculation is rather complicated and computationally burdened as it requires determination of normal vectors to the drop contour in many points and calculating distances along these vectors to the experimental points. Additional inconvenience may arise from the representation form of experimental data points:

for the computational procedure to be reliable, the normal vectors to the calculated drop contour always must target the corresponding point in the experimental one.

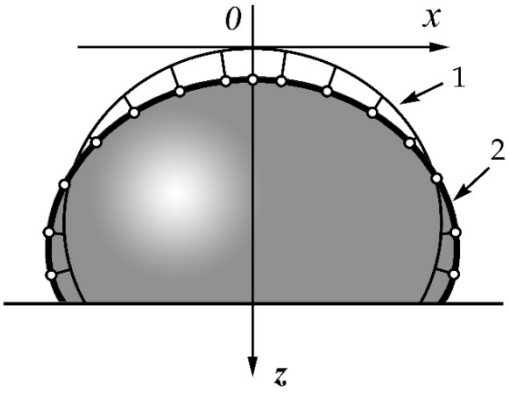

Fig. 14. Calculation of the objective function which quantifies the discrepancy between the calculated Laplacian contour of the drop (*1*) and the experimental points (*2*)

Over these and other problems, the ADSA method has undergone various improvements since it had been presented in its initial version. In [139], a streamlined version of the development of ADSA over the past several decades is presented to illustrate its validity and range of utility. Numerous related approaches have been proposed, similar in tasks to the ADSA method [140–148]. Factors influencing precision of sessile drop method when used for determination of surface tension and contact angle are analysed in [149, 150].

Basics of image processing techniques for determination of drop contours.

As follows from the above, the methods intended for determination of surface tension, contact angle, surface energy of solid, and other values accessible through the analysis of the sessile drop shape require the drop contour to be singled out in the image. Contours characterise the physical extent of objects, and their accurate detection plays a key role in problems related to image analysis. These problems arise in computer vision and its applications related to pattern recognition in various fields ranging from cartography and processing of aerial and space surveying data [151] to tomography-based techniques for medical diagnostics [152–154].

The contour of the digital image is composed by its pixels, which are located in the area of a sharp change in the luminance function. The operation performing selection of contours should result in identification of these pixels. Most of algorithms implementing this operation can roughly be divided into two categories. One of them relies upon calculating the derivative of the luminance function, while another one traces the boundary by "crawling" along the consecution of boundary pixels between two image regions which have distinctions in luminance. The first category is commonly referred to as "edge detectors", or "boundary detectors", while another one is termed "boundary tracing", or "contour tracing". The essential difference between the two is that the edge detectors highlight any luminance discontinuity regardless of the general topology of the image, while the boundary tracer is designed to delineate closed regions possessing some distinguishing features. Both methods can be implemented for assessment of the contact angle, however, in our opinion, the later one has the advantage of an implicit parameterization of the revealed contour pixels by their ordering.

Several edge detectors have been proposed in literature for enhancing and detecting edges in images. The simplest technique for determining the contours is the spatial differentiation of the luminance function. Among the most used contour detection algorithms using spatial differentiation are the Sobel operator [155], the Roberts cross operator [156], the Laplacian edge detector [157], and the Prewitt edge detection technique [158]. For instance, the Sobel edge detector was used for the axisymmetric drop shape analysis (ADSA) in [155, 160].

The algorithms mentioned above have many similarities. To outline briefly the idea behind these algorithms, consider the Laplacian edge detector, which has an advantage of independency on the boundary direction. The Laplace function can be presented in the following form:

$$L(x,y)=\frac{d^2f}{dx^2}+\frac{d^2f}{dy^2} \quad . \tag{68}$$

For discrete functions of two variables, which represent images, the second derivatives can be approximated by finite differences with the coefficients written as a matrix function. For instance, the Sobel differentiating operator can be represented in matrix form by two matrix transformations:

$$\mathbf{P}=\begin{vmatrix}+1 & +2 & +1\\ 0 & 0 & 0\\ -1 & -2 & -1\end{vmatrix};\quad \mathbf{Q}=\begin{vmatrix}+1 & 0 & -1\\ +2 & 0 & -2\\ =1 & 0 & -1\end{vmatrix}. \tag{69}$$

Then the value of the gradient can be calculated according to the expression:

$$G=\sqrt{p^2+q^2}, \tag{70}$$

where p, q are results of operations (67) on the image.

Among the edge detection methods developed so far, one of the most strictly defined methods is the Canny edge detection algorithm that provides good and reliable detection [161]. As a purpose, Canny have formulated three criteria to be met by an optimal operator for step edge detection: good detection, good localization, and only one response to a single edge. Owing to its optimality to meet with these criteria and the simplicity of process for implementation, the Canny algorithm became one of the most popular edge detectors. It organizes the points at which image brightness changes sharply into a set of curved line segments. In particular, this method was employed for extracting the edge of the sessile drop, which was then used in comparative evaluation of four different techniques designed to measure apparent contact angles of non-axisymmetric drops [162]. However, various factors like reflection of light, shadows, or illumination heterogeneity result in discontinuities of the detected contours, which put obstacles when using these contours in fitting procedures. An example of edges detected using Canny algorithm is illustrated in Figs. 15 *a*, *b*. Current state and prospects of further improvement of edges detection algorithms are discussed in [163].

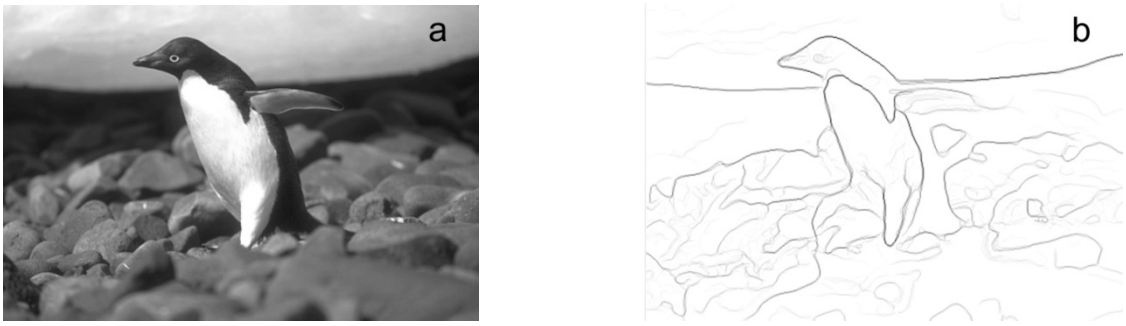

Fig. 15. An example of edges detected using Canny algorithm. The raw half tone image (*a*) and the extracted contours (*b*). Note that many contours are open-ended

Consider now algorithms that realise contour tracing. One of the earliest approaches to extracting contours in the image was the square tracing algorithm (STA). It was quite simple and capable of extracting contours only when the image does not contain half tones and can be represented by a binary pattern. Its idea is traditionally explained by example of the ladybird's[2] trajectory when it moves along the edge of continuous area (Fig. 16). The algorithm begins from locating the image pixel that belongs to the boundary (the start pixel). The ladybird standing on the start pixel turns left, and every time it finds herself standing on a white pixel, turns right, until it encounters the start pixel again. The image pixels it walked over will be the contour of the pattern.

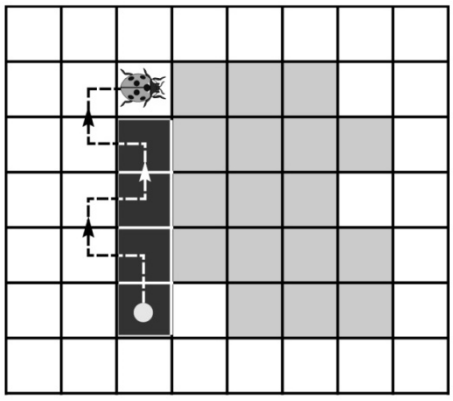

Fig. 16. Extraction of contour in binary image using the square tracing algorithm

[2] Ladybird (*Coccinellidae*) is a widespread family of small beetles ranging in size from 0.8 to 18 mm.

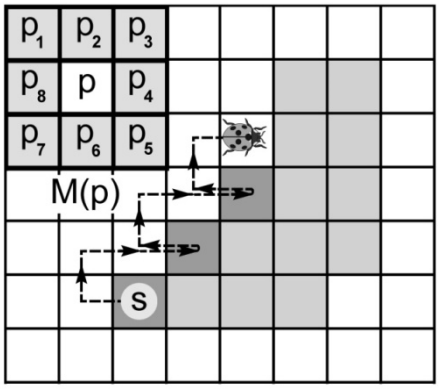

Fig. 17. Contour tracing using Moore algorithm. The traced contour pixels are shown shadowed

Another approach to tracing the contours is known as the Moore neighbour tracing algorithm [164]. To explain this method, we define first an important concept of the Moore neighbourhood of a pixel. The Moore neighbourhood, $M(p)$ (also known as the 8-neighbors or indirect neighbours) is the set of eight pixels around the central pixel p. After having located the start pixel, s at the boundary of the image, the algorithm proceeds with testing in series the pixels that belong to its Moore neighbourhood, as shown in Fig. 17. The general idea consists in the following: every time the pixel under test appeared to be the image pixel (grayed), the "ladybird" backtracks (*i.e.* goes back to the white pixel previously visited), then goes around the new central pixel in a clockwise direction, visiting each pixel in its Moore neighbourhood until hits another grayed pixel. The algorithm terminates when the start pixel is visited for a second time.

Actually, both the above algorithms are impractical for extracting contours of real images obtained with the video camera, as their boundaries inevitably contain half tones. These algorithms were described here just to give understanding of general principles of contour detection. Realistic procedures should involve preliminary enhancement of image contrast, smoothing noise, and detection (or tracing) the contours with more elaborated algorithms capable of managing the half-tone pixels. An example of practical approach to measuring the contact angles from digital images of liquid drops is described, for instance, by M. Mirzaei [165]. For a comprehensive learning the subject of contour extraction techniques, readers are advised to refer to dedicated monographs [166, 167].

INSTRUMENTATION FOR CONTACT ANGLE MEASUREMENTS USING THE SESSILE DROP METHOD

As noted above, at present the research and technological areas where the measurement of surface wettability and contact angle is highly important are rapidly expanding. In response to this tendency, manufacturers offer nowadays a broad line of instruments, which meet a wide variety of technical requirements: from the simplest models of primary and educational level to perfect highly automated systems suitable for scientific research of the highest complexity (Table). Technical characteristics of several contact angle analyzers produced by the well-known manufacturers are considered below in more detail.

Among the manufacturers indicated in the above Table, the ramé-hart instrument co. deserves special attention. It was this US-basing company, which developed the world's first mass produced contact angle goniometer ramé-hart Model A100 (see Fig. 9). This instrument and its successor, Model 100-00, enjoyed a useful lifespan of nearly fifty years with thousands units produced during this time. Many hundreds of them are still in use today throughout the world.

Currently, ramé-hart produces about a dozen of different models and their modifications. Among the entry-level instruments, the device that attracts attention is the goniometer Model 90 CA Edition [168], which is optimized for contact angle measurement. The 90 CA Edition includes a DROPimage CA as well as a German-made SuperSpeed U3 series digital camera with a resolution of 1920×1080 pixels, LED illumination (fiber optic upgrade available), sample alignment stage and high modulus optical bench.

The professional instrument, Model 790 (Fig. 18) [169] is a research-grade device, which is one of the most powerful and feature-rich in this class equipment. This model includes automated tilting, automated dispensing, oscillation, high-speed camera (210 fps), environmental control from –50 °C to 300 °C, and optical overhead imaging. Powered by DROPimage Advanced software, Model 790 can measure static contact angle, dynamic contact angle, surface energy, work of adhesion, surface tension, interfacial tension, surface dilatational

viscosity and elasticity. The system is a complete turn-key setup and ships ready to plug-and-play. Conceptually, the contemporary ramé–hart instruments inherit the classic design of the Model A100, where different units were installed on the optical bench. An evident advantage of this design is its easiness in adaptation to different measurement conditions and research tasks, which can be accomplished simply by replacing correspondent units.

Table. Commercially available instrumentation for contact angle measurements

Manufacturer's name / brand, location, web site	Instrument models
ramé-hart instrument co. 19 Route 10 East, Suite 11,Succasunna, NJ 07876 USA http://www.ramehart.com	Models 90, 210, 250, 260, 290, 400, 500, 590, 790.
KRÜSS Scientific. Hamburg, Germany https://www.kruss-scientific.com/en/	DSA 25, DSA 100 (different modifications).
Biolin Scientific/Attention®. Headquarter in Gothenburg, Sweden https://www.biolinscientific.com/attension	Optical tensiometers: Theta Flow, Theta Flex (different modifications)
Kyowa Interface Science Co. Ltd. 5-4-41 Nobitome, Niiza-City, Saitama 352-0011, Japan Tel: +81-48-483-2629, Fax: +81-48-483-2702 Email: overseas-sales@face-kyowa.co.jp https://www.face-kyowa.co.jp/english/	Contact angle meters. DropMaster series: DMe -211, DMs -401, DMo (series) DMo –WA (series) Devices: PCA-4, MCA-4; FAMAS Software
Holmarc Opto-Mechatronics Pvt. Ltd. B.7, HMT Rd, Industrial Estate, P.O, Kalamassery, Kochi, Kerala 683503, India https://holmarc.com/contact_angle_meter.php	Models: HO-IAD-CAM-01, HO-IAD-CAM-01A, HO-IAD-CAM-01B, HO-IAD-CAM-01BC, HO-IAD-CAM-LLE
DataPhysics Instruments. DataPhysics Instruments GmbH, Raiffeisenstraße 34, 70794 Filderstadt, Germany https://www.dataphysics-instruments.com/	**OCA series– Optical contact angle measuring and contour analysis systems:** OCA 15EC, OCA 15LJ, OCA 25
Ossila. Solpro Business Park, Windsor Street, Sheffield, S4 7WB +44 (0)114 2999 180. Email: info@ossila.com (Founded in 2009 by organic electronics research scientists) https://www.ossila.com/pages/about	Product Code L2004A1 Price £1,500.00 (≈57000 UAN)
Open Science LLC NPK. 143444, Moscow region, Krasnogorsk, Russia.	Goniometer LK-1

Another world leader in development of instrumentation intended for surface studies, KRÜSS Scientific, places particular emphasis on the greatest possible user comfort for their customers. One of their most elaborated devices, Drop Shape Analyser Model DSA 100, combines high scientific demands with ever-simpler operating concepts achieved due to intense use of computer control and dedicated software for data analysis [170]. This instrument, equipped with the ADVANCE software, perfectly exemplifies this approach: the system measures the contact angle and surface free energy (SFE) using easy to create measuring procedures with the highest degree of automation possibilities. Due to this high level of automation, the DSA 100 is an optimal choice as the instrument for quality control, for instance, in the analysis of cleaned, pre-treated or coated solid materials. A simpler device from the same manufacturer is the Drop Shape Analyzer DSA30 model. In its basic version, the DSA30 is intended for the accurate determination of wettability using the static contact angle measurements. Fast and simple exchange of solid samples and dosing liquids makes this instrument especially convenient for evaluating the effectiveness of cleaning procedures or the quality of coating and wetting processes. Optionally, this instrument can be equipped with

accessories for wetting measurements at higher temperatures. The range of its applications can be enlarged with various available upgrade options. More details on its performances are outlined in [171].

Performances of other instruments listed in Table are generally intermediate between the simplest and most advanced instruments discussed here. We refer the readers to the provided links for more details.

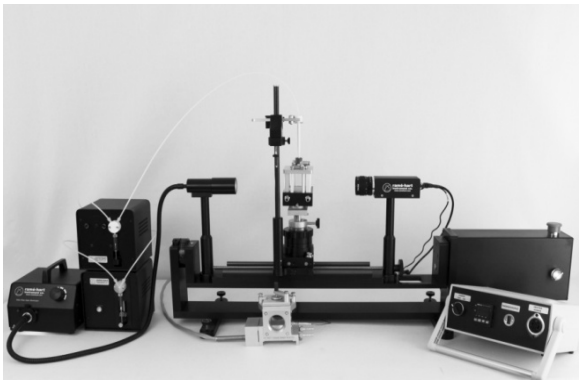

Fig. 18. The ramé-hart Model 790 contact angle goniometer

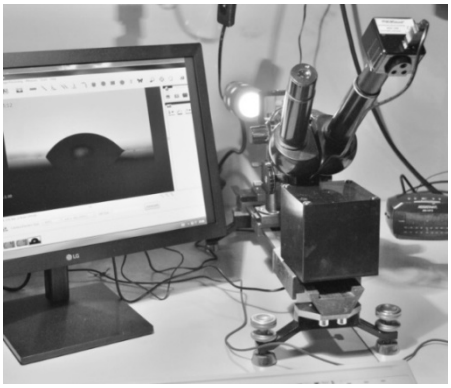

Fig. 19. The prototype contact angle analyser designedt at V.Ye. Lashkariov Institute of semiconductor physics (NASU)

A prototype contact angle analyser intended for testing technical solutions and software is currently under development at V.Ye. Lashkariov Institute of Semiconductor Physics (NASU) (Fig. 19). Similarly to the ramé-hart instruments, it implements a modular design including the optical bench and replaceable modules for installing the samples under study. It is assumed to be used, depending on the task at hand, to study the processes of both non-reactive and reactive wetting. The reactive wetting is involved, in particular, into formation of interconnecting solder bumps for assembling the multielement hybride focal planes, which are employed as sensor devices for infrared vision. The non-reactive wetting characteristics are of crucial importance in developing the diagnostic kits for biomedical applications, which are based on the enzyme-linked immunosorbent assay (ELISA) principles.

CONCLUDING REMARKS

In this review, we presented a cumulative coverage of different issues related to wettability and its investigation. The discussed topics include the basic concepts of wetting as a physical phenomenon, the most common methods for its characterisation (with an emphasis on the sessile drop technique), and the general overview of contemporary instruments for wettability measurements. A distinctive feature of these measurements as a tool for surface research is that they provide a direct quantitative assessment of the interactions between the surface under study and the wetting liquid, expressed either through surface forces or through surface energy. The wettability measurements can be performed in real time and under different experimental conditions, allowing the study of various transient phenomena often encountered during wetting. They can also contribute to investigation of interfacial chemistry of solids by the use of wetting fluids of different physical properties and/or incorporating different functional groups. Typical applications of wettability measurements, usually in combination with the surface-sensitive analytical techniques are aimed at assessing surface properties relevant to a specific research purpose or application. The efficiency of this method is evidenced by continuously growing area of its applications over the past decades.

The topics outlined in this review were restricted mainly to theoretical and experimental approaches concerning stationary measurements on a homogeneous surface. Many other significant issues that go beyond the basic concepts were left outside the consideration. To guide the reader interested in deeper understanding of the subject, we refer him to some of these issues that complement the scope of this review.

– The surface of a solid, like a liquid, is characterized by increased potential energy compared to the volume and presence of corresponding surface tension. However, in contrast to a liquid, the bulk stiffness of a solid prevents it from changing its geometry under the surface tension forces. Therefore, in general, the surface tension of solids cannot be measured directly (with the exception of specially prepared specimens). The problem can be resolved by the measurements of wettability, which, in addition to the interaction forces between a liquid and the surface of a solid (or other liquid), also make it possible to estimate the surface energy of solids [172, 173].

– Besides the ADSA method for analysing the results of wettability measurements, another related technique was proposed for extraction of contact angle based on the sessile drop experiments. This technique, termed Theoretical Image Fitting Analysis (TIFA), relies on processing the image directly at a pixel level, which eliminates the need for an independent edge detection procedure and simplifies the algorithm as a whole [174, 175].

– As has long been known, the measurements of the contact angle under stationary conditions can be influenced by surface roughness, inhomogeneous wetting characteristics, or other factors, which can lead to ambiguous results. This problem can be mitigated by resorting to a technique that uses dynamic contact angle measurements. In this approach, the volume of the drop is first gradually increased by the supply of liquid, and then decreased, with the corresponding sequence of drop images being recorded. The following analysis takes into account both the advancing and receding contact angles, as well as the observed hysteresis between them [87, 176–179].

There are many other important issues related to wetting. They include the effect of surface diffusion and the effect of surfactants, reactive wetting, interfacial chemical reactions, interdiffusion and other irreversible processes between a wetting liquid (including melts) and a solid surface. Most of them, as being complicated by involvement of additional concomitant effects apart from wetting, were not touched upon in this review. On these and other issues, we refer the reader to more specialized literature.

Змочуваність поверхні та кут змочування: фізичні основи та методи дослідження

Г.В. Бекетов, О.В. Шинкаренко

Інститут фізики напівпровідників ім. В.Є. Лашкарьова Національної академії наук України
пр. Науки, 41, Київ, 03028, Україна, gbeketov@ukr.net

Характеристика змочуваності поверхні має вирішальне значення у багатьох галузях науки і технології, від видобувної промисловості до створення сучасних функціональних матеріалів і виробів біомедичного призначення. Зростаючий інтерес до явищ, пов'язаних зі змочуваністю, стимулює стрімке зростання дослідницької діяльності в цьому напрямку. Метою представленого огляду є послідовне висвітлення низки питань, пов'язаних з природою змочуваності та методами її дослідження. В ньому розглядаються базові концепції змочуваності як фізичного явища, методи для кількісного визначення її характеристик та сучасний рівень приладів для визначення характеристик змочуваності.

У першому розділі розглядаються фізичні основи змочуваності. Міжмолекулярні взаємодії, якими обумовлюється змочуваність, класифікуються залежно від їхньої природи. Так, обговорення міжмолекулірних взаємодій, у яких беруть участь полярні молекули, охоплює взаємодії між молекулами, які мають постійний дипольний момент, включаючи особливий механізм взаємодії між молекулами, який виникає, коли молекули можуть вільно обертатися. Розгляд взаємодій, що відбуваються в результаті поляризації молекул, включає взаємодії між іонами та незарядженими молекулами, взаємодії Дебая та дисперсійні сили Лондона. Водневі зв'язки розглядаються як окремий тип взаємодій.

У другому розділі розглядаються питання, які стосуються поверхневого натягу та його впливу на форму поверхні рідини, яка знаходиться у контакті з твердим тілом. Обговорюється взаємозв'язок між

величиною поверхневого натягу та значенням контактного кута змочування. Розглядається рівняння Юнга-Лапласа, яке визначає форму краплі рідини, яка лежить на твердій поверхні.

Третій розділ присвячений експериментальному визначенню характеристик змочуваності поверхні та теоретичним засадам відповідних методів вимірювання. Особлива увага приділяється методу, відомому в англомовній літературі як метод ADSA, який засновується на аналізі форми краплі, що лежить на поверхні. Коротко розглядаються чисельні методи виявлення геометричних структур на оцифрованих зображеннях, які призначені для отримання кількісних даних про силу поверхневого натягу та значення крайового кута змочування.

У четвертому розділі наводиться огляд приладів для дослідження змочуваності та вимірювання крайового кута, які серійно випускаються приладобудівельними підприємствами у різних країнах світу. Представлений також прототип приладу аналогічного призначення, створений у ІФН НАНУ.

***Ключові слова**: змочуваність, міжмолекулярні взаємодії, поверхневий натяг, крайовий кут змочування, крапля, що лежить, рівняння Юнга-Лапласа, аналіз форми вісесиметричної краплі, гоніометрія крайового кута змочування, виділення контурів на цифрових зображеннях, методи оптимізації*

REFERENCES

1. Nogalska A., Trojanowska A., Tylkowski B., Garcia-Valls R. Surface characterization by optical contact angle measuring system. *Phys. Sci. Rev*. 2019. **5**(2): 20190083.
2. Woodruff D.P. *Modern techniques of surface science. 3rd ed.* (Cambridge: Cambridge University Press, 2016).
3. Yun W., Chang S., Cogswell D.A., Eichmann S.L., Gizzatov A., Thomas G., Al-Hazza N., Abdel-Fattah A., Wang W. Toward reservoir-on-a-chip: rapid performance evaluation of enhanced oil recovery surfactants for carbonate reservoirs using a calcite-coated micromodel. *Sci. Rep.* 2020. **10**: 782.
4. Tajmiri M., Zallaghi M., Roozbehani B. A comprehensive review of chemically induced reservoir wettability alteration: characterization and EOR aspects. *Am. J. Oil Chem. Technol.* 2018. **6**(2): 151.
5. Mohammed M., Babadagli T. Wettability alteration: A comprehensive review of materials/methods and testing the selected ones on heavy-oil containing oil-wet systems. *Adv. Colloid Interface Sci*. 2015. **220**: 54.
6. Erzuah S., Fjelde I., Omekeh A.V. Wettability characterization using the flotation technique coupled with geochemical simulation. In: *European Symposium on Improved Oil Recovery (IOR 2017)*. Proc. 19th Int. Conf. (Apr. 24, 2017, Stavanger, Norway). P. 1.
7. Chi J., Zhang X., Wang Y., Shao C., Shang L., Zhao Y. Bio-inspired wettability patterns for biomedical applications. *Mater. Horiz*. 2021. **8**(1): 124.
8. Xue M., Ji Y., Ou J., Wang F., Li C., Lei S., Li W. Surface wettability and strong adhesion of medical polyurethane elastomer porous films by microphase separation. *AIP Adv*. 2019. **9**(7): 075309.
9. Nychka J.A., Gentleman M.M. Implications of wettability in biological materials science. *JOM*. 2010. **62**(7): 39.
10. Menzies K.L., Jones L. The impact of contact angle on the biocompatibility of biomaterials. *Optometry and Vision Science*. 2010. **87**(6): 387.
11. Campbell D., Carnell S.M., Eden R.J. Applicability of contact angle techniques used in the analysis of contact lenses, part 1: comparative methodologies. *Eye Contact Lens*. 2013. **39**(3): 254.
12. Read M.L., Morgan P.B., Kelly J.M., Maldonado-Codina C. Dynamic contact angle analysis of silicone hydrogel contact lenses. *J. Biomater. Appl.* 2011. **26**(1): 85.
13. Cai S., Wu C., Yang W., Liang W., Yu H., Liu L. Recent advance in surface modification for regulating cell adhesion and behaviors. *Nanotechnol. Rev.* 2020. **9**(1): 971.
14. Cai Q., You H., Guo H., Wang J., Liu B., Xie Z., Chen D., Lu H., Zheng Y., Zhang R. Progress on AlGaN-based solar-blind ultraviolet photodetectors and focal plane arrays. *Light. Sci. Appl*. 2021. **10**: 94.
15. Motmaen A., Rostami A., Matloub S. Ultra high-efficiency integrated mid infrared to visible upconversion system. *Sci. Rep.* 2020. **10**: 9325.
16. Rogalski A., Antoszewski J., Faraone L. Third-generation infrared photodetector arrays. *J. Appl. Phys.* 2009. **105**(9): 091101.
17. Law K.Y., Zhao H. Contact angle measurements and surface characterization techniques. In: *Surface Wetting*: *Characterization, Contact Angle, and Fundamentals*. (Cham: Springer, 2016).
18. De Wijs W.J.A., Laven J., de With G. Wetting forces and meniscus pinning at geometrical edges. *AIChE J*. 2016. **62**(12): 4453.
19. Zimon A.D. *Fluid adhesion* and *wetting*. (Moscow: Chemistry, 1974). [in Russian].

20. Padday J.F., Uffindell N.D. The calculation of cohesive and adhesive energies from intermolecular forces at a surface. *J. Phys. Chem.* 1968. **72**(5): 1407.
21. Kumar G., Prabhu K.N. Review of non-reactive and reactive wetting of liquids on surfaces. *Adv. Colloid Interface Sci.* 2007. **133**(2): 61.
22. Weltsch Z. Wetting of non-reactive and reactive metallic substrates by brazing liquids. *IOP Conf. Ser.: Mater. Sci. Eng.* 2020. **903**(1): 012035.
23. Eustathopoulos N. Wetting by liquid metals - application in materials processing: the contribution of the Grenoble Group. *Metals.* 2015. **5**(1): 350.
24. Young T. An Essay on the Cohesion of Fluids. *Philosophical Transactions of the Royal Society of London.* 1805. **95**: 65.
25. Israelachvili J.N. *Intermolecular and surface forces*. 3rd ed. (Amsterdam: Elsevier, 2011).
26. Barash Yu.S. *Van der Waals forces.* (Moscow: Nauka. 1988). [In Russian].
27. Prigogine I. The molecular theory of solutions. (Amsterdam: North-Holland publishing company, 1957).
28. Rimai D.S., Quesnel D.J. Particle adhesion. In: *Adhesion science and engineering.* V. 2. (Amsterdam: Elsevier B.V., 2002).
29. Margenau H., Kestner N.R. *Theory of intermolecular forces.* (Oxford: Pergamon. 1971).
30. Israelachvili J.N. Van der Waals forces in biological systems. *Q. Rev. Biophys.* 1974. **6**(4): 341.
31. Mahanty J., Ninham B.W. *Dispersion forces*. (New York: Academic Press. 1976).
32. Parsegian V.A. *Van der Waals forces: a handbook for biologists, chemists, engineers, and physicists.* (New York: Cambridge University Press, 2006).
33. Pauling L. *The nature of the chemical bond and the structure of molecules and crystals; an introduction to modern structural chemistry.* 3rd ed. (Ithaca (NY): Cornell University Press, 1960).
34. Coulson C.A. *Valence.* 2nd ed. (New York: Oxford University Press, 1961).
35. Joesten M.D., Schaad L.J. *Hydrogen bonding*. (New York: Dekker, 1974).
36. Jeffrey G.A. *An introduction to hydrogen bonding (topics in physical chemistry)*. (USA: Oxford University Press, 1997).
37. Schuster P., Zundel G., Sandorfy C. *The hydrogen bond.* (Amsterdam: North-Holland Publ., 1976).
38. Steiner T. The hydrogen bond in the **s**olid **s**tate. *Angew. Chem. Int. Ed.* 2002. **41**(1): 48.
39. Larson J.W., McMahon T.B. Gas-phase bihalide and pseudobihalide ions. An ion cyclotron resonance determination of hydrogen bond energies in XHY- species (X, Y = F, Cl, Br, CN). *Inorg. Chem.* 1984. **23**(14): 2029.
40. Emsley J. Very strong hydrogen bonds. *Chem. Soc. Rev.* 1980. **9**(1): 91.
41. Needham P. Hydrogen bonding: Homing in on a tricky chemical concept. *Studies in History and Philosophy of Science. Part A.* 2013. **44**(1): 51.
42. Inoue M. Structural integrity of metal–polymer adhesive interfaces in microelectronics. In: *Advanced Adhesives in Electronics. Materials, Properties and Applications*. (Sawston, Cambridge: Woodhead Publishing, 2011).
43. Hutchins K.M. Functional materials based on molecules with hydrogen-bonding ability: applications to drug co-crystals and polymer complexes. *R. Soc. Open Sci.* 2018. **5**(6): 180564.
44. Zhang J., Zeng H. Intermolecular and Surface Interactions in Engineering Processes. *Engineering.* 2021. **7**(1): 63.
45. Dzialoshinskii I.E., Lifshiz E.M., Pitaevskii L.P. General theory of van der Waals forces. *Uspekhi Fizicheskih Nauk.* 1961. **LXXIII**(3): 381. [in Russian].
46. Hermann J., Robert A., DiStasio Jr. R.A., Tkatchenko A. First-principles models for van der Waals interactions in molecules and materials: Concepts, theory, and applications. *Chem. Rev.* 2017. **117**(6): 4714.
47. Leite F.L., Bueno C.C., Da Róz A.L., Ziemath E.C., Oliveira Jr.O.N. Theoretical models for surface forces and adhesion and their measurement using atomic force microscopy. *Int. J. Mol. Sci.* 2012. **13**(10): 12773.
48. Singla S., Jain D., Zoltowski C.M., Voleti S., Stark A.Y., Niewiarowski P.H., Dhinojwala A. Direct evidence of acid-base interactions in gecko adhesion. 2021. *Sci. Adv.* **7**(21): eabd9410.
49. Whitesides G.M., Biebuyck H.A., Folkers J.P., Prime K. Acid-base interactions in wetting. *J. Adhes. Sci. Technol.* **5**(1): 57.
50. Casimir H.B.C. On the attraction between two perfectly conducting plates. *Proc. K. Ned. Akad. Wet*. 1948. **51**(7): 793.
51. Drosdoff D., Woods L.M. Casimir forces and graphene sheets. *Phys. Rev. B*. 2010. **82**(15): 155459.
52. Bordag M., Fialkovsky I.V., Gitman D.M., Vassilevich D.V. Casimir interaction between a perfect conductor and graphene described by the Dirac model. *Phys. Rev. B.* 2009. **80**(24): 0245406.
53. Fialkovsky I.V., Marachevsky V.N., Vassilevich D.V. Finite temperature Casimir effect for graphene. *Phys. Rev. B.* 2011. **84**(3): 035446.
54. Adamson A.W., Gast A.P. *Physical chemistry of surfaces. 6th ed*. (New York: A Wiley Interscience Publication, 1997).

55. Hebbar R.S., Isloor A.M., Ismail A.F. Contact Angle Measurements. In: *Membrane Characterization.* (Amsterdam: Elsevier, 2017).
56. *Ebnesajjad S., Landrock A.H.* Surface Tension and Its Measurement. *In: Adhesives Technology Handbook.* 3rd ed. *(Amsterdam:* Elsevier Inc., 2015*).*
57. Van Oss C.J. Chapter Two - The apolar and polar properties of liquid water and other condensed-phase materials. *Interface Science and Technology. Book series.* 2008. **16**: 13.
58. Dupré A. *Theorie mécanique de la chaleur.* (Paris: Gauthier-Villars, 1869).
59. Durand M. Mechanical approach to surface tension and capillary phenomena. *American Journal of Physics.* 2021. **89**(3): 261.
60. Adam N.K. *The physics and chemistry of surfaces. 3rd ed.* (London: Oxford University Press, 1941).
61. Bangham D.H., Razouk R.I. Adsorption and wettability of solid surfaces. *Trans. Faraday Soc.* 1937. **33**: 1459.
62. *Zisman W.A.* Relation of the equilibrium contact angle to liquid and solid constitution. In: *Contact angle, wettability, and adhesion.* (Washington: American Chemical Society, 1964).
63. Good R.J. Contact angle, wetting, and adhesion: a critical review. *J. Adhes. Sci. Technol*. 1992. **6**(22): 1269.
64. Bikerman J.J. *Surface Chemistry.* 2nd ed. (New York: Academic Press, 1958).
65. Bikerman J.J. Surface energy of solids. *Top. Curr. Chem*. 1978. **77**: 1.
66. Ivanov I.B., Kralchevsky P.A., Nikolov A.D. Film and line tension effects on the attachment of particles to an interface: I. Conditions for mechanical equilibrium of fluid and solid particles at a fluid interface. *J. Colloid Interface Sci. 1*986. **112** (1): 97.
67. Johnson R.E.Jr. Conflicts between Gibbsian thermodynamcis and recent treatments of interfacial energies in solid-liquid-vapor systems. *J. Phys. Chem.* 1959. **63**(10): 1655.
68. Gao L., McCarthy T.J. Wetting 101. *Langmuir.* 2009. **25**(24): 14105.
69. Makkonen L. Faulty intuitions of wetting. *International Journal of Wettability Science and Technology*. 2018. **1**(1): 13.
70. Hui C.Y., Jagota A. Deformation near a liquid contact line on an elastic substrate. *Proc. Math. Phys. Eng. Sci.* 2014. **470**(2167): 20140085.
71. Makkonen L. Young's equation revisited. *J. Phys.: Condens. Matter.* 2016. **28**(13): 135001.
72. Frumkin A.N. On wetting and sticking phenomena. *Zhurnal Fizicheskoi Khimii.* 1938. **12**(4): 337. [in Russian].
73. Derjaguin B.V. Theory of capillary condensation and other capillary phenomena accounting for the disjoining pressure of polymolecular liquid films. *Acta Physicochimia.* 1940. **12**(2): 181. [in Russian].
74. Derjaguin B.V., Zorin Z.M. Study of the surface condensation and adsorption of vapors near saturation by the optical micropolarization method. *Zhurnal Fizicheskoi Khimii.* 1955. **29**(10): 1755. [in Russian].
75. Lubarsky G.V., Davidson M.R., Bradley R.H. Particle-surface capillary forces with disjoining pressure. *Phys. Chem. Chem. Phys.* 2006. **8**(21): 2525.
76. Van Honschoten J.W., Brunets N., Tas N.R. Capillarity at the nanoscale. *Chem. Soc. Rev.* 2010. **39**(3): 1096.
77. Popescu M.N., Oshanin G., Dietrich S., Cazabat A.M. Precursor films in wetting phenomena. *J. Phys.: Condens. Matter*. 2012. **24**(24): 243102.
78. Indekeu J.O. Line tension at wetting. *Int. J. Mod. Phys. B.* 1994. **8**(3): 309.
79. Hirasaki G.L. Wettability: Fundamentals and Surface Forces. *SPE Form Eval*. 1991. **6**(02): 217.
80. Boruvka L., Neumann A.W. Generalization of the classical theory of capillarity. *J. Chem. Phys.* 1977. **66**(12): 5464.
81. Saini D., Rao D.N. Line Tension-Based Modification of Young's Equation for Rock-Oil-Brine Systems. *SPE Reservoir. Eval. Eng.* 2009. **12**(05): 702.
82. Li D., Neumann A.W. Determination of line tension from the drop size dependence of contact angles. *Colloids Surf*. 1990. **43**(2): 195.
83. Koshoridze S.I. Calculating Line Tension for a Simple Model of a Surface Nanobubble. *Tech. Phys. Lett.* 2020. **46**(5): 416.
84. Das S.K., Egorov S.A., Virnau P., Winter D., Binder K. Do the contact angle and line tension of surfaceattached droplets depend on the radius of curvature? *J. Phys.: Condens. Matter.* 2018. **30**(25): 255001.
85. Weijs J.H., Marchand A., Andreotti B., Lohse D., Snoeijer D.J. Origin of line tension for a Lennard-Jones nanodroplet. *Phys. Fluids.* 2011. **23**(2): 022001.
86. Drelich J.W., Boinovich L., Chibowski E., Della Volpe C., Hołysz L., Marmur A., Siboni S. Contact angles: history of over 200 years of open questions. *Surf. Innovations.* 2020. **8**(1–2): 3.
87. Tadmor R. Line energy and the relation between advancing, receding, and young contact angles. *Langmuir.* 2004. **20**(18): 7659.
88. Swain P.S., Lipowsky R. Contact angles on heterogeneous surfaces: A new look at Cassie's and Wenzel's laws. *Langmuir.* 1998. **14**(23): 6772.
89. Cassie A.B.D., Baxter S. Wettability of porous surfaces. *Trans. Faraday Soc*. 1944. **40**: 546.

90. Cassie A.B.D. Contact angles. *Discuss. Faraday Soc.* 1948. **3**: 11.
91. Wenzel R.N. Resistance of solid surfaces to wetting by water. *Ind. Eng. Chem*. 1936. **28**(8): 988.
92. Wolansky G., Marmur A. Apparent contact angles on rough surfaces: the Wenzel equation revisited. *Colloids Surf. A.* 1999. **156**(1–3): 381.
93. Marmur A. Soft Contact: Measurement and Interpretation of Contact Angles. *Soft Matter.* 2006. **2**: 12.
94. Kung C.H., Sow P.K., Zahiri B., Mérida W. Assessment and interpretation of surface wettability based on sessile droplet contact angle measurement: challenges and opportunities. *Adv. Mater. Interfaces.* 2019. **6**(18): 1900839.
95. Eral H.B., Oh J.M. Contact angle hysteresis: A review of fundamentals and applications. *Colloid Polymer Sci.* 2013. **291**(2): 247.
96. Moradi S., Englezos P., Hatzikiriakos S.G. Contact angle hysteresis: surface morphology effects. *Colloid Polymer Sci.* 2013. **291**(2): 317.
97. Bormashenko E.Y. *Physics of wetting. Phenomena and applications of fluids on surfaces.* (Boston: Cengage Learning - Gale, 2017).
98. Mugele F., Heikenfeld J. Introduction to capillarity and wetting phenomena. In: *Electrowetting: Fundamental Principles and Practical Applications.* 1st ed. (Weinheim: Wiley-VCH Verlag GmbH & Co. KGaA, 2019).
99. Siqveland L.M., Skjæveland S.M. Derivations of the Young-Laplace equation. *Capillarity*. 2021. **4**(2): 23.
100. Yuan Y., Lee T.R. Contact Angle and Wetting Properties. In: *Surface Science Techniques*. (Berlin Heidelberg: Springer-Verlag, 2013).
101. Volpe C.D., Siboni S. The Wilhelmy method: a critical and practical review. *Surf. Innovations*. 2018. **6**(3): 120.
102. Lu C., Wang J., Lu X., Zheng T., Liu Y., Wang X., Zhang D., Seveno D. Wettability and Interfacial Properties of Carbon Fiber and Poly(ether ether ketone) Fiber Hybrid Composite. *ACS Appl. Mater. Interfaces*. 2019. **11**(34): 31520.
103. Yum K., Yu M.-F. Measurement of Wetting Properties of Individual Boron Nitride Nanotubes with the Wilhelmy Method Using a Nanotube-Based Force Sensor. *Nano Lett.* 2006. **6**(2): 329.
104. Bruel C., Queffeulou S., Darlow T., Nick Virgilio N., Tavares J.R., Patience G.S. Experimental Methods in Chemical Engineering: Contact Angles. *Can. J. Chem. Eng.* 2018. **97**(4): 832.
105. Hebbar R.S., Isloor A.M., Ismail A.F. Contact Angle Measurements. In: *Membrane Characterization.* (Amsterdam: Elsevier, 2017).
106. Law K.Y., Zhao H. *Surface Wetting. Characterization, Contact Angle, and Fundamentals.* (Cham: Springer International Publishing, 2016).
107. *Shimokawa M., Takamura T.* Relation between *interfacial* tension and capillary liquid rise on polished metal electrodes. *J. Electroanal. Chem. Interfacial Electrochem*. 1973. **41**(3): 359.
108. Budziak C.J., Vargha-Butler E.I., Neumann A.W. Temperature dependence of contact angles on elastomers. *J. Appl. Polym. Sci*. 1991. **42**(7): 1959.
109. Jordan D.D., Lane J.E. A thermodynamic discussion of the use of a vertical-plate balance for the measurement of surface tension. *Austral. J. Chem.* 1964. **17**(1): 7.
110. Budziak C.J., Neumann A.W. Automation of the capillary rise technique for measuring contact angles. *Colloids Surf.* 1990. **43**(2): 279.
111. Restagno F., Poulard C., Cohen C., Vagharchakian L., Léger L. Contact angle and contact angle hysteresis measurements using the capillary bridge. *Langmuir.* 2009. **25**(18): 11188.
112. Vagharchakian L., Restagno F., Léger L. Capillary bridge formation and breakage: A test to characterize antiadhesive Surfaces. *J. Phys. Chem. B.* 2009. **113**(12): 3769.
113. Cohen C., Restagno F., Poulard C., Léger L. Wetting and dewetting transition: An efficient toolbox for characterizing low-energy surfaces. *Langmuir.* 2010. **26**(19): 15345.
114. Adam N.K., Jessop G.J. Angles of contact and polarity of solid surfaces. *J. Chem. Soc., Trans.* 1925. **127**: 1863.
115. Extrand C.W., Moon S.I. Indirect Methods to Measure Wetting and Contact Angles on Spherical Convex and Concave Surfaces. *Langmuir.* 2012. **28**(20): 7775.
116. Bigelow W.C., Pickett D.L., Zisman W.A. Oleophobic Monolayers. I. Films adsorbed from Solution in Non-Polar. Liquids. *J. Colloid Sci.* 1946. **1**(6): 513.
117. Neumann A.W., Good R.J. Methods of measuring contact angles. In: *Surface and Colloid Science: Experimental Methods*. V. 11. (New York: Plenum Publishing, 1979).
118. Hunter R.J. *Foundations of Colloid Science*. 2nd ed. (Oxford: Clarendon Press, 2001).
119. Quincke G.H. Ueber der capillaritats-erscheinungen an der gemeinschaftlichen Oberfläche von Flüssigkeiten. *Annu. Phys. Chem*. 1870. **215**: 1.
120. Magie W.F. The contact angle of liquids and solids. *Philos. Mag*. 1888. **26**: 162.
121. de Gennes P.G., Brochard-Wyart F., Quere D. *Capillarity and Wetting Phenomena: Drops, Bubbles, Pearls, Waves.* (New York: Springer, 2004).

122. Behroozi F. Determination of contact angle from the maximum height of enlarged drops on solid surfaces. *Am. J. Phys.* 2012. **80**(4): 284.
123. Williams D.L., Kuhn A.T., Amann M.A., Hausinger M.B., Konarik M.M., Nesselrode E.I. Computerized Measurement of Contact Angles. *Galvanotechnik*. 2010. **101**(11): 2502.
124. Behroozi F., Behroozi P.S. Reliable determination of contact angle from the height and volume of sessile drops. *Am. J. Phys*. 2019. **87**(1): 28.
125. Bunday B.D. *Basic optimisation methods.* (London: Edward Arnold, 1984).
126. Rotenderg Y., Boruvka L., Neumann A.W. Determination of surface tension and contact angle from the shapes of axisymmetric fluid interfaces. *J. Colloid Interface Sci.* 1983. **93**(1): 169.
127. Bashforth F., Adams J.C. *An attempt to test the theories of capillary attraction*. (Cambridge: Cambridge University Press, 1883).
128. Euler L. Recherches sur la courbure des surfaces. *Mémoires de l'Académie des Sciences de Berlin.* 1767. **16**: 119.
129. Eisenhart L.P. *A treatise on the differential geometry of curves and surfaces*. (Boston: Ginn and Company, 1909).
130. Glaeser G., Stachel H., Odehnal B. *The Universe of Conics: From the ancient Greeks to 21st century developments*. (Berlin Heidelberg: Springer Spektrum, 2016).
131. Yates R.C. *Analytic geometry with calculus.* (New Jersey: Englewood Cliffs, 1961).
132. Muskhelishvili N.I. *Analytic Geometry Course, 4th edition*. (Moskow: Vysshaya shkhola, 1967). [in Russian].
133. Protter M.H., Morrey C.B. *College calculus with analytic geometry*. (Boston: Addison-Wesley, 1970).
134. Kishan H. *Differential calculus*. (New Dehli: Atlantic Publishers and Distributors, 2007).
135. Zhang Y., Chatain D., Anna S.L., Garoff S. Stability of a Compound Sessile Drop at the Axisymmetric Configuration. *J. Colloid Interface Sci.* 2016. **462**: 88.
136. Zhu Z.Q., Wang Y., Liu Q.S., Xie J.C. Influence of Bond number on behaviors of liquid drops deposited onto solid substrates. *Microgravity Sci. Technol.* 2012. **24**(3): 181.
137. Hartland S., Hartley R.W. *Axisymmetric fluid-liquid interfaces*. (Amsterdam: Elsevier, 1976).
138. Ferguson R. An easier derivation of the curvature formula from first principles. *Australian senior mathematics journal.* 2018. **32**(2): 16.
139. Saad S.M.I., Neumann A.W. Axisymmetric Drop Shape Analysis (ADSA): An outline. *Adv. Colloid Interface Sci.* 2016. **238**: 62.
140. Del Río O.I., Neumann A.W. Axisymmetric Drop Shape Analysis: Computational Methods for the Measurement of Interfacial Properties from the Shape and Dimensions of Pendant and Sessile Drops. *J. Colloid Interface Sci.* 1997. **196**: 136.
141. Bateni A., Susnar S.S., Amirfazli A., Neumann A.W. A high-accuracy polynomial fitting approach to determine contact angles. *Colloids Surf. A.* 2003. **219**(1–3): 215.
142. Atefi E., Mann J.A., Tavana H. A Robust Polynomial Fitting Approach for Contact Angle Measurements. *Langmuir*. 2013. **29**(19): 5677.
143. Cabezas M.G., Bateni A., Montanero J.M., Neumann A.W. A new drop-shape methodology for surface tension measurement. *Appl. Surf. Sci.* 2004. **238**(1–4): 480.
144. Stalder A.F., Melchior T., Müller M., Sage D., Blu T., Unser M. Low-bond axisymmetric drop shape analysis for surface tension and contact angle measurements of sessile drops. *Colloids Surf. A.* 2010. **364**(1–3): 72.
145. Kalantarian A., David R., Chen J., Neumann A.W. Simultaneous measurement of contact angle and surface tension using axisymmetric drop-shape analysis-no apex (ADSA-NA). *Langmuir.* 2011. **27**(7): 3485.
146. Hussain R., Vogt S.J., Honari A., Hollingsworth K.G., Sederman J., Mitchell J., Johns M.L. Interfacial tension measurements using MRI drop shape analysis. *Langmuir*. 2014. **30**(6): 1566.
147. Marchuk I.V., Cheverda V.V., Strizhak P.A., Kabov O.A. Determination of surface tension and contact angle by the axisymmetric bubble and droplet shape analysis. *Thermophys. Aeromech.* 2015. **22**(3): 297.
148. Heib F., Schmitt M. Statistical contact angle analyses with the high-precision drop shape analysis (HPDSA) approach: Basic principles and applications. *Coatings.* 2016. **6**(4): 57.
149. Yang J., Yu K., Zuo Y.Y. Accuracy of axisymmetric drop shape analysis in determining surface and interfacial tensions. *Langmuir.* 2017. **33**(6): 8914.
150. Vuckovac M., Latikka M., Liu K., Huhtamäki T., Ras R.H.A. Uncertainties in contact angle goniometry. *Soft Matter.* 2019. **15**: 7089.
151. Ma W.Y., Manjunath B.S. Edgeflow: a technique for boundary detection and image segmentation. *IEEE Trans. Image Process*. 2000. **9**(8): 1375.
152. Somkantha K., Theera-Umpon N., Auephanwiriyakul S. Boundary detection in medical images using edge following algorithm based on intensity gradient and texture gradient features. *IEEE Trans. Biomed. Eng*. 2011. **58**(3): 567.
153. Senthilkumaran N., Vaithegi S. Image segmentation by using thresholding techniques for medical images. *Comput. Sci. Eng.* 2016. **6**(1): 1.

154. Sharma N., Aggarwal L.M. Automated medical image segmentation techniques. *J. Med. Phys.* 2010. **35**(1): 3.
155. Danielsson P.E., Seger O. Generalized and separable sobel operators. In: *Machine vision for three-dimensional scenes.* (Cambridge: Academic Press, 1990).
156. Davis L.S. A survey of edge detection techniques. *Computer Graphics and Image Processing.* 1975. **4**(3): 248.
157. Mlsna P.A., Rodríguez J.J. Chapter 19 - Gradient and Laplacian Edge Detection. In: *The essential guide to image processing.* 2nd ed. (Cambridge: Academic Press, 2009).
158. Adlakha D., Adlakha D., Tanwar R. Analytical Comparison between Sobel and Prewitt Edge Detection Techniques. *International Journal of Scientific & Engineering Research (IJSER).* 2016. **7**(1): 1482.
159. Hoorfar M., Neumann A.W. Axisymmetric drop shape analysis (ADSA) for the determination of surface tension and contact angle. *The Journal of Adhesion.* 2004. **80**(8): 727.
160. Hoorfar M., Neumann A.W. Recent progress in axisymmetric dop shape analysis (ADSA). *Adv Colloid Interface Sci*. 2006. **121**(1–3): 25.
161. Canny J.F. A computational approach to edge detection. *IEEE Transactions on Pattern Analysis and Machine Intelligenc*e. 1986. **8**(6): 769.
162. Biole D., Wang M., Bertola V. Assessment of direct image processing methods to measure the apparent contact angle of liquid drops. *Exp. Therm. Fluid Sci*. 2016. **76**: 296.
163. Zakariah M., AlShalfan K., Li D., Huang W., Xu G., Zhang T., Shahnasser H. Image boundary, corner, and edge detection: past, present, and future. *International Journal of Computer Electrical Engineering.* 2020. **12**(2): 39.
164. Teja V.S.M., Rao K.D.G. Moore contour tracing algorithm. *Int. Res. J. Eng. Technol*. 2019. **6**(9): 1330.
165. Mirzaei M. A new method for measuring the contact angles from digital images of liquid drops. *Micron.* 2017. **102**: 65.
166. Sonka M., Hlavac V., Boyle R. *Image Processing, Analysis, and Machine Vision.* 4th ed. (Stamford: Cengage Learning, 2015).
167. Szeliski R. *Computer Vision: Algorithms and Applications*. (New York: Springer, 2011).
168. Ramé-hart Model 90 Goniometer / Tensiometer. http://ramehart.com/pdf/90_Series.pdf
169. Ramé-hart Model 790. http://ramehart.com/pdf/790.pdf
170. The KRÜSS Scientific Drop Shape Analyzer DSA100 model. https://www.kruss-scientific.com/en/products-services/products/dsa100m
171. The KRÜSS Scientific Drop Shape Analyzer DSA30 model (Datasheet). https://www.kruss-scientific.com/en/products-services/products/dsa30b
172. Owens D.K., Wendt R.C. Estimation of the surface free energy of polymers. *J. Appl. Polym. Sci.* **13** (8): 1741.
173. Palencia M. Surface free energy of solids by contact angle measurements. *J. Sci. Technol. Appl*. 2017. **2**: 84.
174. Cabezas M.G., Bateni A., Montanero J.M., Neumann A.W. A new drop-shape methodology for surface tension measurement. *Appl. Surf. Sci.* 2004. **238**(1–4): 480.
175. Cabezas M.G., Bateni A., Montanero J.M., Neumann A.W. A new method of image processing in the analysis of axisymmetric drop shapes. *Colloids Surf. A*. 2005. **255**(1): 193.
176. Eral H.B., 't Mannetje D.J.C.M., Oh J.M. Contact angle hysteresis: a review of fundamentals and applications. *Colloid Polym. Sci.* 2013. **291**(2): 247.
177. Makkonen L. A thermodynamic model of contact angle hysteresis. 2017. *J. Chem. Phys.* **147**(6): 064703.
178. Chibowski E., Jurak M. Comparison of contact angle hysteresis of different probe liquids on the same solid surface. *Colloid Polym. Sci.* 2013. **291**(2): 391.
179. Huhtamäki T., Tian X., Korhonen J.T., Ras R.H. A. Surface-wetting characterization using contact-angle measurements. *Nature Protocols*. 2018. **13**(7): 1521.

Received 16.08.2021, accepted 03.03.2022